Tesi doctoral presentada per En/Na

Marc MANERA MIRET

amb el títol

"Cosmologia i Formació d'Estructures"

per a l'obtenció del títol de Doctor/a en

CIÈNCIES FÍSIQUES

Barcelona, 27 de juny del 2007.

Facultat de Física
Departament de Física Fonamental

UNIVERSITAT DE BARCELONA

Part II

Structure Formation through Cross-Correlating Sky Maps

Chapter 9

The Integrated Sachs-Wolfe Effect

Summary

In this chapter I present the Integrated Sachs Wolfe Effect (ISW) and how it can be detected through cross-correlation between CMB-temperature maps and large scale structure surveys. The cross-correlation analysis can be done either in configuration or in spherical harmonic space. I also show the redshift and cosmological parameter dependences of the ISW kernel, which is the key contribution to the signal.

9.1   The ISW Effect and the growth of structure

The ISW effect (Sachs & Wolfe 1967) has emerged as a new and powerful tool to probe the (linear) rate of structure formation in our universe on the largest physical scales, testing deviations from General Relativity and the existence of dark-energy independent of other classical probes like supernovae distances (Crittenden & Turok 1996; Bean & Dore 2004; Lue et al. 2004b; Cooray et al. 2004; Garriga et al. 2004; Song et al. 2006) The ISW secondary anisotropies in the CMB appear because of the net gravitational redshifts affecting CMB photons that travel through an evolving gravitational potential Φ. These secondary temperature anisotropies are therefore correlated with local, evolving, structures on large scales. For a flat universe without dark energy (Einstein-de-Sitter cosmology) there is no cross-correlation signal because the gravitational potential remains constant, despite the linear growth of matter fluctuations. The correlation is negative when the structures grow faster

83

than in the Einstein-de-Sitter cosmology, because the increasing potential blueshifts photons and leaves a cold spot in the CMB sky. Otherwise the correlation is positive.

The rate of structure formation in the universe can also be measured by galaxy peculiar velocities or galaxy redshift distortions, on very large scales through the so-call β parameter determination (Peacock et al. 2001; Pope et al. 2004). The ISW effect provides an independent and complementary probe of the same effect. Independent, because it uses temperature anisotropies instead of the velocity field, and complementary, because of the different assumptions and systematics that relate measurements with theory. Despite recent advances in the size of galaxy redshift surveys such as SDSS and 2dFGRS, the spectrum of matter fluctuations $P(k) \propto < \delta(k)^2 >$ is quite difficult to measure directly over very large scales (Gaztanaga 1998; Percival et al 2001; Tegmark et al. 2004). Part of the problem is that matter correlations fall quickly to zero on scales larger than 30 Mpc/h ($k < 0.1$ h/Mpc). In contrast, fluctuations in the gravitational potential go as $\Phi(k) \propto \delta(k)/k^2$ and therefore extend over larger distances, which makes the signal more detectable. The ISW cross-correlation traces the gravitational potential, Φ, and thus provides a new window to study the largest structures, extending over several degrees in the sky or tens of Mpc/h at the survey depth.

The ISW temperature anisotropies are given by

$$\Delta_T^{ISW}(\hat{n}) = -\int_0^{z_i} dz \frac{d}{dz}(\Phi - \Psi) = -\int_0^{z_i} 2dz \frac{d\Phi}{dz}(\vec{r}(\hat{n}), z) \tag{9.1}$$

where Φ and Ψ are the Newtonian gauge gravitational potentials ($\Phi = -\Psi$ for isotropic stress), and z_i is a redshift well inside the radiation era.

9.2 Detecting ISW though cross-correlation of sky maps in configuration space

The detection of ISW can be achieved through cross-correlating CMB temperature maps with dark matter fluctuations as traced by galaxy surveys. The sky (2D) linear galaxy fluctuations are related to the 3D linear dark matter fluctuations though an integral weighted by the normalized galaxy selection function of the survey $\phi(z)$ and the local deterministic bias $b(z)$, which relates the matter

fluctuations to galaxy ones. This is:

$$\delta_g(\hat{n}) = \int dz\, b(z)\phi(z)\delta_m(\vec{r}, z) = \int dz\, W_G(z)\delta_m^0(\vec{r}, z_0) \tag{9.2}$$

where $\hat{n}$ is a given direction in the sky and δ_m^0, is the current linear dark matter density fluctuation at comoving position $\vec{r} = |\vec{r}|\hat{n}$. Here we have introduced the galaxy kernel $W_G = b(z)\phi(z)D(z)$ where $D(z)$ is the linear growth factor (normalized to be one at z=0).

In this section we are interested in the cross-correlation $w_{TG}(\theta) =< \Delta_T^{ISW}(\hat{n})\, \delta_g(\hat{n}') >_\theta$, where $< ... >_\theta$ is an average of all sky points separated an angle θ, $\hat{n}\hat{n}'= \theta$. In order to compute w_{TG} it is easier to work in Fourier space.

$$\delta_m(\vec{r}, z) = \int \frac{d^3\vec{k}}{(2\pi)^3}e^{i\vec{k}\vec{r}}\delta_m(\vec{k}, z) \tag{9.3}$$

$$\Phi(\vec{r}, z) = \int \frac{d^3\vec{k}}{(2\pi)^3}e^{i\vec{k}\vec{r}}\Phi(\vec{k}, z) = \int \frac{d^3\vec{k}}{(2\pi)^3}e^{i\vec{k}\vec{r}}\left(-\frac{3}{2}\right)\frac{H_0^2}{c^2k^2}\Omega_m\frac{D(z)}{a}\delta_m(\vec{k}, z_0) \tag{9.4}$$

In the last equation we related the gravitational potential Φ to the density fluctuation by means the Poisson equation $\nabla^2\Phi = 4\pi Ga^2\bar{\rho}_m\delta_m$, which in Fourier space reads as $\Phi(\vec{k}, z) = -\frac{3}{2}\frac{H_0^2}{c^2k^2}\Omega_m\frac{D(z)}{a}\delta_m(\vec{k}, z_0)$. This will allow us to express the cross-correlation in terms of the power spectrum. Lets first for simplicity define the ISW kernel as $W_{ISW} = 3\frac{H_0^2}{c^2}\Omega_m\frac{d}{dz}\left(\frac{D(z)}{a}\right)$. This kernel is plotted in figure 9.1 for the Λ CDM cosmology with different values of Ω_m and Ω_Λ. Using this we get

$$\Delta_T^{ISW}(\hat{n}) = \int dz\, W_{ISW}(z)\int \frac{d^3\vec{k}}{(2\pi)^3k^2}e^{i\vec{k}\vec{r}}\delta_m(\vec{k}, z_0) \tag{9.5}$$

Now we can write the angular cross-correlation as

$$\begin{aligned}
w_{TG}(\theta) &= < \Delta_T^{ISW}(\hat{n})\, \delta_g(\hat{n}') >_\theta \\
&= \int dz \int dz' W_G(z)W_G(z')\int \frac{d^3\vec{k}}{(2\pi)^3}e^{i\vec{k}\vec{r}}\int \frac{d^3\vec{k}'}{(2\pi)^3k'^2}e^{i\vec{k}'\vec{r}'} < \delta_m(\vec{k}, z_0), \delta_m(\vec{k}', z_0) >
\end{aligned} \tag{9.6}$$

where we have use the ergodic theorem to express the average over the sample points in the sky in an average over realizations. The power spectrum $P(k)$ at $z = 0$ is defined as $< \delta_m(\vec{k}, z_0), \delta_m(\vec{k}', z_0) >=$
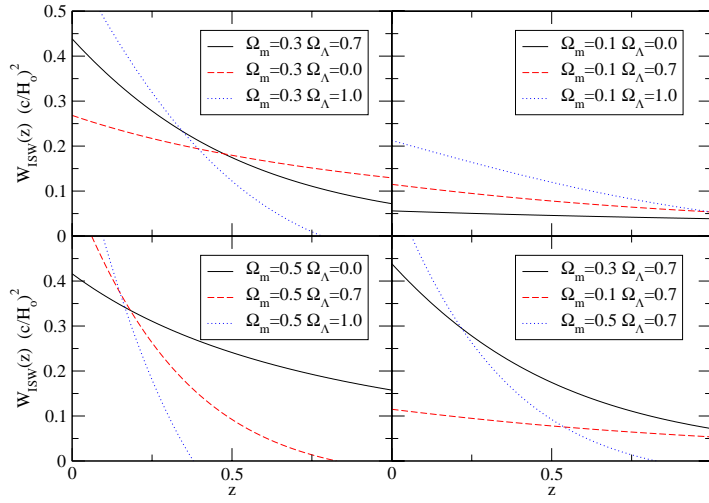
Figure 9.1: Redshift dependence of $W_{ISW}(z)$ in Eq. 9.11 for different values of Ω_m and Ω_Λ. Bottom left, top right and top left panels shows a fixed $\Omega_m = 0.5$, $\Omega_m = 0.3$ and $\Omega_m = 0.1$ respectively. In all cases: $\Omega_\Lambda = 0.0$ (dotted blue line) , $\Omega_\Lambda = 0.7$ (continuous black line) and $\Omega_\Lambda = 1.0$ (dashed red line). Bottom right panel shows a fixed $\Omega_\Lambda = 0.7$ and $\Omega_m = 0.3$ (continuous black line), $\Omega_m = 0.5$ (dotted blue line) and $\Omega_\Lambda = 0.1$ (dashed red line). Figure from Gaztanaga, Manera & Multamaki (2006).

$P(k)(2\pi)^3\delta^D(\vec{k} + \vec{k}')$, thus we get

$$
\begin{aligned}
w_{TG}(\theta) &= \int dz dz' W_G(z) W_{ISW}(z') \int \frac{d^3\vec{k}}{(2\pi)^3 k^2} e^{i\vec{k}(\vec{r}-\vec{r}')} P(k) & (9.7) \\
&= \int dz dz' W_G(z) W_{ISW}(z) \frac{1}{(2\pi)^2} \int_0^\infty dk \int_0^\pi d\theta \sin(\theta) e^{ik|\vec{r}-\vec{r}'|\cos(\theta)} P(k) & (9.8) \\
&= \int dz dz' W_G(z) W_{ISW}(z') \frac{2}{(2\pi)^2} \int_0^\infty dk \frac{\sin(k|\vec{r}-\vec{r}'|)}{k|\vec{r}-\vec{r}'|} P(k) & (9.9)
\end{aligned}
$$

We proceed by exchanging the order of the integrals, and performing a change of variables from redshift to comoving transverse distances $dr = c\, dz/H(z)$. We separate the two integrals over r and r' by further changing the variables to $s = r - r'$ and $r_m = (r + r')/2$. We make use of the small separation $r \simeq r' \simeq r_m$ and small angle ($\theta \ll 1$) approximation $|\vec{r} - \vec{r}'| = \sqrt{r^2 + r'^2 - 2rr'\cos(\theta)} \simeq$

$\sqrt{s^2 + r_m^2 \theta^2}$. After that we arrive to

$$w_{TG}(\theta) = \int_0^\infty dk \frac{2}{(2\pi)^2} P(k) \int dr_m W_G(z) W_{ISW}(z) \frac{H^2(z)}{c^2} \int_{-2r_m}^{2r_m} \frac{\sin(k\sqrt{s^2 + r_m^2 \theta^2})}{k\sqrt{s^2 + r_m^2 \theta^2}} \quad (9.10)$$

where $z = z(r_m)$. While being in the regime where $r_m \gg \frac{1}{k\theta}$ we can extend the limits of the last integral to $\pm\infty$, (see eg. (Garriga et al. 2004)) and its result will be $\frac{\pi}{k} J_0(kr_m\theta)$, where J_0 is the zero-order Bessel function. Going back to an integration over redshift we get the final equations for the ISW cross-correlation.

$$\begin{aligned}
w_{TG}^{ISW}(\theta) &= \frac{1}{2\pi} \int \frac{dk}{k} P(k) g(k\theta) \\
g(k\theta) &= \int dz\, W_{ISW}(z) W_G(z) \frac{H(z)}{c} J_0(k\, r_m \theta) \\
W_{ISW}(z) &= 3\Omega_m (H_0/c)^2 \frac{d[D(z)/a]}{dz} \\
W_G(z) &= b(z) \phi_G(z) D(z),
\end{aligned} \quad (9.11)$$

The power spectrum is $P(k) = A\, k^{n_s}\, T^2(k)$, where $n_s \simeq 1$ [1] and $T(k)$ is the Λ CDM transfer function. In chapter 10 we will evaluate T(k) using the fitting formulae of Einseinstein & Hu (1998). For the ΛCDM case the ISW effect is non-zero, and the kernel W_{ISW} can be written as $W_{ISW}(z) = -3\Omega_m (H_0/c)^2 D(z)(f-1)$, where f is the relative growth factor $f = d\ln(D)/d\ln(a)$ and can be well approximated by $f \simeq \Omega_m(z)^{6/11}$. W_{ISW} decreases as a function of increasing redshift and goes to zero both for $\Omega_m \to 0$ and for $\Omega_m \to 1$. At low redshifts, the ISW effect is larger for larger values of Ω_m, but the redshift evolution depends on how quickly the H and D evolve respect to the EdS case. This is illustrated in Fig.9.2 which shows how W_{ISW} depends on z for different values of Ω_Λ and Ω_m. At high redshifts, the lower the value of Ω_Λ (for a fixed Ω_m) the larger the ISW amplitude. In Figures 9.2 and 9.3 we also show for a given flat cosmology model the dependence of the W_{ISW} on redshift and on the equation of state parameter w. For a given redshift and Ω_m there exists a maximum of W_{ISW} around $w = -0.5$. This maximum would translate into a maximum in the cross-correlation signal w_{TG}. If data turns out to be greater than this maximum this would clearly disfavor models with constant equation of state.

---

[1] This is the assumption, expected by inflation, of scale invariant primordial fluctuations ($n_s \simeq 1$), for other possibilities see, eg, (Barriga et al. 2001).
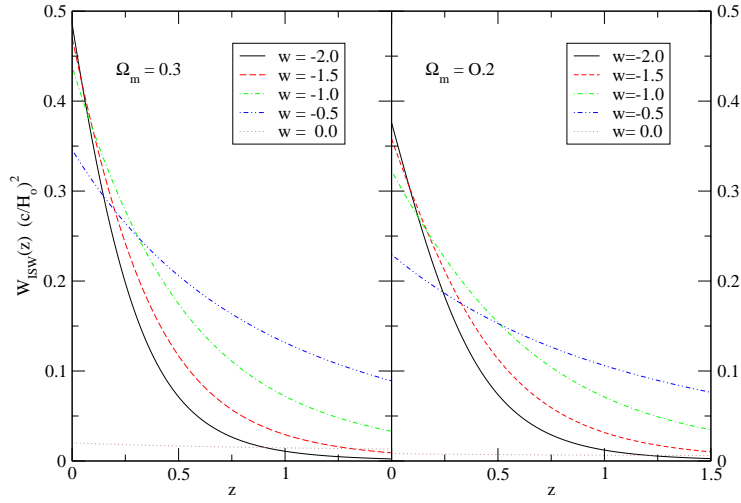
Figure 9.2: Redshift dependence of W_{ISW} in eq 9.11 for flat models with constant equation of state. Right panel shows a fixed $\Omega_m = 0.2$ and left panel $\Omega_m = 0.3$. In both cases $w = -2$ (black continuous line), $w = -1.5$ (red dashed line), $w = -1$ (green dot-dashed line), $w = -0.5$ (blue doubledot-dashed line), and $w = 0$ (brown dotted line). Figure from Gaztanaga, Manera & Multamaki (2006).
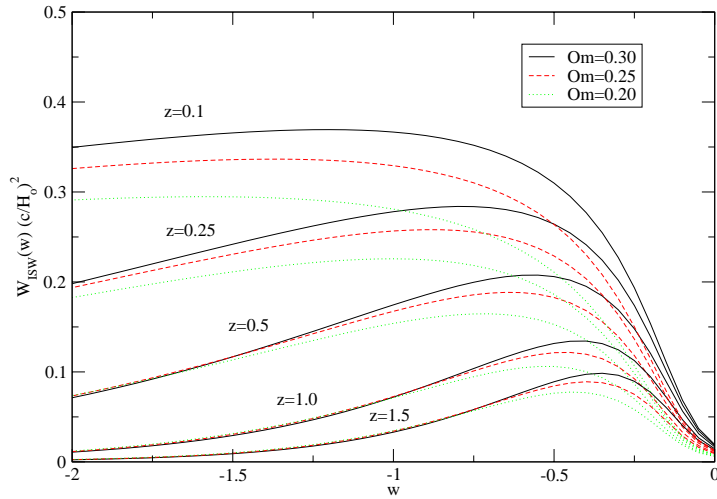

Figure 9.3: Dependence of W_{ISW} on the equation of state parameter w for flat models at different redshifts and values of Ω_m. $\Omega_m = 0.3$ (back continuous lines), $\Omega_m = 0.25$ (red dashed lines), $\Omega_m = 0.2$ (green dotted lines). Redshifts are 0.1, 0.25, 0.5, 1.0, 1.5 from top to bottom. Figure from Gaztanaga, Manera & Multamaki (2006).

It is worth to notice that the galaxy auto-correlation function can be also computed by the same means as in equation 9.11 but changing the ISW kernel by the galaxy one W_G.

9.3 Cross-Correlation of two sky fields in harmonic space

In the last section we discussed the detection of ISW effect by cross-correlating sky maps in configuration space. Alternatively one may choose to cross-correlate the maps in the spherical harmonic space. For doing so one has to choose a coordinate basis for the spherical harmonics and express the fields of the sky as a function of them. Consider a field in the sky, $\tilde{A}$, we will have

$$\tilde{A}(\hat{n}) = \sum_{lm} \tilde{A}_{lm} Y_{lm}(\hat{n}) \quad \Rightarrow \quad \tilde{A}_{lm}(\hat{n}) = \int Y_{lm}^*(\hat{n}) \tilde{A}(\hat{n}) d\hat{n} \tag{9.12}$$

This field can be also expressed as an integration over a selection function $F_A(r)$ of the 3D field $A(\vec{x})$

$$\tilde{A}(\hat{n}) = \int dr F_A(r) A(r\hat{n}) \quad A_k = \int d^3x e^{-i\vec{k}\vec{x}} A(\vec{x}) \tag{9.13}$$

where in the last equation we wrote the Fourier transform of the 3D field. Armed with these ingredients we can compute the cross-correlation of two fields in harmonic space

$$C_{AB}(l) \equiv < \tilde{A}_{lm} \tilde{B}_{lm}^* >$$
$$= \int d\hat{n} d\hat{n}' Y_{lm}^*(\hat{n}) Y_{lm}(\hat{n}') \int dr dr' F_A(r) F_B(r') \int \frac{d^3k_1 d^3k_2}{(2\pi)^6} e^{i\vec{k}_1\vec{r}} e^{-i\vec{k}_2\vec{r}} < A_{k_1} B_{k_2}^* > \tag{9.14}$$

Now we can introduce the power spectrum $< A_{k_1} B_{k_2}^* >= (2\pi)^3 \delta^D(k_1-k_2) P_{AB}(k_1)$ and also expand the exponentials using the wave expansion, $e^{i\vec{k}\vec{r}} = 4\pi \sum_{lm} i^l j_l(\vec{k}\vec{r}) Y_{lm}(\hat{n}) Y_{lm}^*(\hat{k})$, thus we get

$$C_{AB}(l) = \int dr dr' F_A(r) F_B(r') \int \frac{d^3k}{(2\pi)^3} P_{AB}(k) \int d\hat{n} d\hat{n}' Y_{lm}^*(\hat{n}) Y_{lm}(\hat{n}')$$
$$\left[4\pi \sum_{l'm'} i^{l'} j_l'(\vec{k}\vec{r}) Y_{l'm'}(\hat{n}) Y_{l'm'}^*(\hat{k}) \right] \left[4\pi \sum_{l''m''} (-i)^{l''} j_l''(\vec{k}\vec{r}) Y_{l''m''}^*(\hat{n}) Y_{l''m''}(\hat{k}) \right] \tag{9.15}$$

which can be simplified by using the spherical harmonic normalization $\int d\hat{n} Y_{lm}^*(\hat{n}) Y_{lm}(\hat{n}') = \delta_{ll'}\delta_{mm'}$ that kills many terms in the sum.

$$
\begin{aligned}
C_{AB}(l) &= \int dr dr' F_A(r) F_B(r') \int \frac{d^3 k}{(2\pi)^3} P_{AB}(k)(4\pi)^2 j_l(\vec{k}\cdot\vec{r}) j_l(\vec{k}\cdot\vec{r}') Y_{lm}^*(\hat{k}) Y_{lm}(\hat{k}) \\
&= \frac{2}{\pi} \int dr dr' F_A(r) F_B(r') \int k^2 \, dk \, j_l(\vec{k}\cdot\vec{r}) j_l(\vec{k}\cdot\vec{r}') P_{AB}(k)
\end{aligned}
\tag{9.16}
$$

This integral requires a lot of computational effort and probes to be unnecessary if we are interested in small angles (or large l's). We can take and approximation of the spherical Bessel function for large multipoles $j_l(x) = \sqrt{\frac{\pi}{2l+1}}\left[\delta^D(l+1/2-x) + \mathcal{O}(l^{-2})\right]$. which will lead us to the Limber equation.

$$
\begin{aligned}
C_{AB}(l) &= \frac{2}{2l+1} \int dr dr' F_A(r) F_B(r') \int dk \, k^2 \frac{\delta\left(\frac{l+1/2}{r}-k\right)}{r} \frac{\delta\left(\frac{l+1/2}{k}-r'\right)}{k} P_{AB}(k) \\
&= \int dr \frac{1}{r^2} F_A(r) F_B(r') P_{AB}\left(\frac{l+1/2}{r}\right)
\end{aligned}
\tag{9.17}
$$

which we have used $\delta(\lambda x - c) = \frac{1}{|\lambda|}\delta(x - c/\lambda)$ Equation 9.17 is the Limber equation, which according to Afshordi et al. (2004) gives an error of 10% at $l = 2$ that then falls as l^{-2}. This approximation will be very useful for the ISW effect since we are only interested in $l \geq 2$ because the dipole have been removed from the WMAP temperature maps and the cross-correlation signal is significant for angles $\theta < 10\,deg$ which corresponds to large multipoles.

When doing the cross-correlation in harmonic space for the ISW effect we would get $P_{\Delta_T,\delta}$ which is not so straightforward to manage. A much better way of performing the cross-correlation is to express the Δ_T in terms of δ as we have done in the previous section. Thus, we will have the standard power spectrum and also introduced a k^2 term which will become $(l+1/2)^2$ after integrating over the delta Dirac functions. If we want to express the cross-correlations with the same kernels as in the previous section we get

$$
\begin{aligned}
C_{GT}^{ISW}(l) &= \frac{4}{(2l+1)^2} \int dz \, W_{ISW}(z) W_G(z) \frac{H(z)}{c} P(k) \\
W_{ISW}(z) &= 3\Omega_m (H_0/c)^2 \frac{d[D(z)/a]}{dz} \\
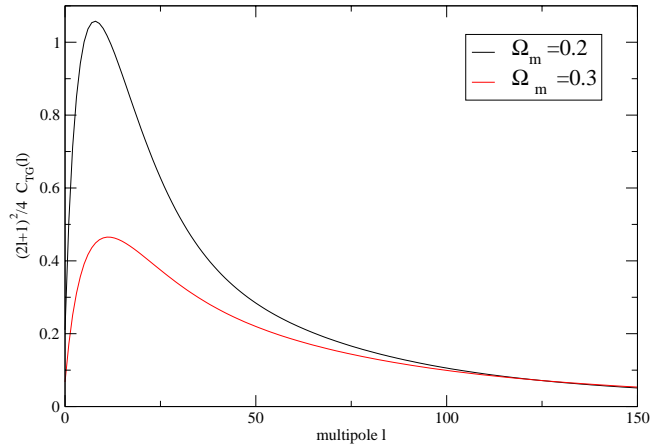W_G(z) &= b(z)\phi_G(z)D(z),
\end{aligned}
\tag{9.18}
$$

Figure 9.4: $C_{TG}(l)$ from the Λ CDM model with $\Omega_m = 0.2$ and $\Omega_m = 0.3$

where again $k = \frac{l+1/2}{r}$, $\phi_G(z)$ is the survey galaxy selection and $r(z)$ is the comoving distance. The factor $H(z)/c$ comes to the change of variables to integrate over redshift. This equations could be understood as a Legendre decomposition of the equations 9.11, which were presented in Fosalba & Gaztañaga (2004) (see also Afshordi 2004). The advantage of this formulation is that we can here set the monopole ($l = 0$) and dipole ($l = 1$) contribution to zero, as it is done in the WMAP maps. The contribution of the monopole and dipole to w_{TG} turns to be significant and over predicts w_{TG} by about 10%.

In figure 9.4 we have plotted $\frac{(2l+1)^2}{4}C_{TG}^{ISW}(l)$ for the Λ CDM cosmology with $\Omega_m = 0.2$ and $\Omega_m = 0.3$ and a galaxy selection function like the SDSS one (see chapter 10). We have used $b = 1$. As expected the correlation is higher for the lower Ω_m. Note how the difference in amplitude changes by a factor of 2 to 3 larger when Ω_m changes only 0.1, illustrating how the ISW effect is very sensitive to cosmological parameters. As it is well known, by using Legendre polynomials, we can recover the correlation function in the configuration space.

$$w_{TG}^{ISW}(\theta) = \sum_l \frac{2l+1}{4\pi} p_l(\cos\theta) C_{GT}^{ISW}(l) \tag{9.19}$$

For completeness we write the result for the autocorrelation function, which is deduced in a same

manner as the cross-correlation.

$$C_{GG}(l) = \int dz \frac{1}{r(z)^2} W_G(z)^2 H(z) P\left(\frac{l+1/2}{r(z)}\right) \tag{9.20}$$

Notice that the formalism in this section has been for an all sky survey, if not a correlation between different modes appear, and one has to introduce window functions. As real large scale surveys do not cover all the sky (usually in the most optimistic case one have to remove the galactic plane), window functions are always needed for experimental treatment of the data. Comments on the effects of coupled modes in harmonic space can be found in chapter 11.

Chapter 10

Fitting Cosmological Parameters with ISW effect

Summary

In this chapter a compilation of ISW observational data for several surveys at different redshifts is presented. These data is used to fit cosmological parameters for the Λ CDM model and also to constrain the dark energy equation of state for flat models. Most of this work is presented as in Gaztanaga, Manera & Multamaki (2006).

10.1   Compiling Observational Data

Several independent collaborations have cross-correlated the CMB anisotropies measured by WMAP with different galaxy surveys and performed and analysis of the ISW signal. The median galaxy redshifts expand over a decade (ie $0.1 < \bar{z} < 1.0$) and trace the matter distribution with light from the whole range of the electromagnetic spectrum: radio, far-infrared, optical and X-ray surveys (see Table 10.1 for the compilation we will use in section 10.3). The cross-correlation and error estimation techniques used are also quite different but they yield comparable results over the scales of interest. Compare for example the Monte Carlo errors to jackknife errors in Fig.3 in Fosalba & Gaztanaga (2004). A detailed discussion on the comparability of error determination will be given in chapters

11 and 12. In our compilation of the different data sets, we average the results on fixed angular scales around $\theta = 6°$. This corresponds to proper distances of $\simeq 25$Mpc/h at $\bar{z} \simeq 0.1$ and $\simeq 100$ Mpc/h at $\bar{z} \simeq 1.0$ in the concordance model and avoids possible contamination from the small scale SZ and lensing effects, eg see Fig. 3 in Fosalba et al. (2003).

Radio galaxies from NVSS (Condon et al. 1998) and hard X-ray background observed by HEAO-1 (Boldt 1987), have been cross-correlated with WMAP data (Boughn & Crittenden 2004b; Boughn & Crittenden 2005), to find a signal of 1.13 ± 0.35 times the concordance model prediction at $z \sim 0.9$. The different biases for X-rays, $b^2 = 1.12$, (Boughn & Crittenden 2004) and for radio galaxies, $b = 1.3 - 1.7$, (Boughn & Crittenden 2002) have been taken into account. A compatible signal has also been found with the NVSS data by the WMAP team (Nolta et al. 2004).

The cross correlation of WMAP with galaxies ($17 < b_J < 20$) in the APM Galaxy Survey (Maddox et al. 1990) (covering about 20% of the South Galactic Cap, SGC) was found to be $w_{TG} = 0.35 \pm 0.13 \, \mu K$ at scales $\theta = 4 - 10°$ with $b \simeq 1$ (Fosalba & Gaztanaga 2004). The cross-correlation of WMAP with the SDSS DR1 (Tegmark et al. 2004) (covering about 10% of the North Galactic Cap, NGC) have been done for several subsamples (Fosalba et al. 2003). The first sample ($\bar{z} \sim 0.3$) contains ~ 5 million objects classified as galaxies in SDSS (with $r < 21$ and low associated error). For this sample, which has $b \simeq 1$, $w_{TG} = 0.26 \pm 0.13 \, \mu K$ at scales $\theta = 4 - 10°$. The high redshift sample ($z \sim 0.5$) has $w_{TG} = 0.53 \pm 0.21 \, \mu K$ and $b^2 \simeq 6$. The SDSS data have also been cross-correlated with WMAP by the SDSS team (Scranton et al. 2003) using nearly 25 million galaxies in four redshift samples. Their results are similar with those obtained earlier by (Fosalba et al. 2003) but no bias from galaxy-galaxy auto correlation function is given. The infrared 2MASS Galaxy Survey (Jarret et al. 2000), with $z \sim 0.1$, show a WMAP cross-correlation of 1.53 ± 0.61 times the Concordance model prediction, with a bias of $b = 1.18$ (Afshordi et al. 2004).

We have selected independent measurements for which the bias for the fiducial model b (from w_{GG}) is known, so that we can apply the bias "self-calibration" proposed in section 10.2. The data is summarized in Table 10.1 and displayed in Fig.1. In the results below we also include a 10% uncertainty in the median redshift. We chose the values of NVSS+HEAO-1 quoted by Boughn & Crittenden (2005) as representative of both the Nolta et al. (2004) and Boughn & Crittenden (2004b) analysis. For the SDSS, we chose the values in Fosalba & Gaztanaga (2004) where the bias b from the concordance model is estimated using the galaxy autocorrelation function (see, eq

$\bar{z}$	w_{TG}/b	b	catalog, Band
0.1	0.70 ± 0.32	1.1	2MASS, infrared ($2\mu m$)
0.15	0.35 ± 0.17	1.0	APM, optical (b_j)
0.3	0.26 ± 0.14	1.0	SDSS, optical (r)
0.5	0.216 ± 0.096	2.4	SDSS high-z, optical (r+colors)
0.9	0.043 ± 0.015	1-2	NVSS+HEAO, Radio & X-rays

Table 10.1: Observed cross correlation w_{TG}/b (averaged for $\theta \simeq 4 - 10°$.) of WMAP anisotropies with different catalogs. Errors in w_{TG}/b includes 20% uncertainty in b. Errors in the median redshift $\bar{z}$ are about 10% .

10.3). Note how the selected samples are complementary. The samples which have large sky overlap (eg 2MASS and NVSS+HEAO-1) have negligible redshift overlap. When the redshift overlap is significant (ie in 2MASS-APM or SDSS-NVSS could be up to 20%) the sky overlap is small (less than 10%). Consequently, the different samples in Table 10.1 have less than 1% volume in common. This is negligible, given that individual sampling errors (which are proportional to volume) are of the order of 30%.

The most significant detection in Table 10.1 seems to be the one quoted by Boughn & Crittenden (2005) for the NVSS+HEAO-1 samples. Given the systematic uncertainties involved in the bias and selection function of both of these samples, we have checked that our results do not changed much (less than 20% in the area of the contours in Fig.3) when we double the quoted errorbar. Doubling this errorbar corresponds to an additional 50% systematic uncertainty in the value b or to a 40% uncertainty in the median redshift of the samples.

The observational data not included in Table 10.1 is in good agreement with the values in the table, but is excluded to avoid redundancy. The agreement of the redundant data provides further confirmation and indicates that errors are dominated by sampling variance rather than by the methodology or the systematics. Data from the table 10.1 was the first compilation of ISW data made in the literature. After its publication it has been used by Corasaniti et al. (2005a) for a related analysis. Since then other groups have also performed cross-correlation analysis. This is the case for the new 2MASS correlation with WMAP (DR3) (Rassat et al. 2006) as well as a NVSS and WMAP3 correlation (Pietrobon et al 2006), which uses spherical wavelet analysis. The redhsift range of the ISW effect detection has also been enlarged to $z \sim 1.5$ by the cross-correlation of WMAP with SDSS quasars (Giannantonio et al. 2006), in which one should take into account the lensing magnification as pointed by Lo Verde et al. (2007).
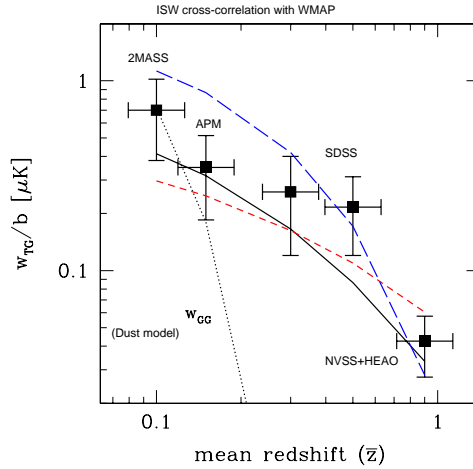
Figure 10.1: Symbols with error bars correspond to the different measurements w_{TG}/b in Table 1. As an illustration of the shape, the continuous, short-dashed and long-dashed lines show the concordance ($\Omega_m = 0.3, \Omega_\Lambda = 0.7$), opened ($\Omega_m = 0.3, \Omega_\Lambda = 0.0$) and closed ($\Omega_m = 0.3, \Omega_\Lambda = 1.1$) model predictions (at $\theta = 6°$). The dotted line corresponds to the galaxy-galaxy prediction (and also the dust contamination model). All lines have arbitrary normalization. Figure from Gaztanaga, Manera & Multamaki (2006).

10.2 Linear growth and bias self-calibration

We are interested to fit the Λ CDM cosmological parameters, as well as the equation of state parameter for a flat cosmology with dark energy, with the redshift evolution of the ISW signal at 6 angular degrees. For the Friedmann equation we will have

$$H^2 = \left(\frac{\dot{a}}{a}\right)^2 = H_0^2 \left[\Omega_m (1+z)^3 + \Omega_\Lambda e^{3 \int_0^z \frac{dz'}{1+z'}(1+w(z'))}\right] \tag{10.1}$$

where $w = -1$ correspond to the standard Λ CDM cosmology. As we have seen the linear growth factor is obtained by solving the linear part of equation 2.21,

$$\frac{d^2 D}{d\eta^2} + \left(2 + \frac{\dot{H}}{H^2}\right)\frac{dD}{d\eta} + 3c_1 \, D = 0, \tag{10.2}$$

where here $c_1 = -\frac{1}{2}\frac{H_0^2 \Omega_m (1+z)^3}{H^2(z)}$ for a constant equation of state parameter w. We will introduce the linear growth in the equations for the ISW correlation 9.11 given in the previous chapter.

The linear bias in these equations is telling us how well light traces the underlying statistics of

linear matter fluctuations. On the very large scales we are probing, fluctuations δ are small and linear theory works very well both for biasing and gravity. We remove the effects of biasing in our parameter estimation by comparing the observed galaxy-galaxy correlation w_{GG}, in the very same samples used for the cross-correlation, to the matter-matter correlation w_{mm} predicted by each model (Fosalba et al. 2003). In fact, we only compiled data in which the observational auto-correlation has been performed, so the bias can be computed using it. The effects of bias are also redshift dependent, but given a galaxy selection function $\phi_G(z)$, picked at $z = \bar{z}$, we approximate the bias with a constant $b = b(\bar{z})$ for that particular survey. We then have: $w_{TG} = b(\bar{z})w_{Tm}$ and $w_{GG} = b^2(\bar{z})w_{mm}$, so that an effective linear bias b can be estimated as the square root of the ratio of galaxy-galaxy and matter-matter correlation functions:

$$b = \sqrt{\frac{w_{GG}}{w_{mm}}}. \tag{10.3}$$

Such prescription has been shown to work well in a variety of galaxy models (eg see (Berlind et al. 2001)). The values of w_{mm} can be computed similar to (9.11) by

$$
\begin{aligned}
w_{mm}(\theta) &= \frac{1}{2\pi} \int dk\, k\, P(k) g(k\theta) \\
g(k\theta) &= \int dz\, W_m^2(z) \frac{H(z)}{c} J_0(k\, r_A \theta) \\
W_m(z) &= \phi_G(z) D(z),
\end{aligned}
\tag{10.4}
$$

where the only difference between W_m and W_G is the bias factor $b(z)$ in equation 9.11. Note how the estimation of b in equation 10.3 depends on the normalization of the power spectrum in w_{mm}. We choose to normalize each model by fixing σ_8. To make our results independent of this normalization we will marginalize over σ_8 and h. Taking flat priors and ranges $\sigma_8 = 0.8 - 1.0$ and $h = 0.72 - 0.77$. We compare the predictions with the observational data w_{TG} normalized to the concordance model bias, ie w_{TG}/b, where b is estimated from equation 10.3 using w_{mm} in the Concordance model. Consequently, for other models, we will need to renormalize each of the theoretical predictions to the Concordance model bias using a "relative bias": $w_{TG}^{mod}/b = b_r\, w_{tm}^{mod}$, where $b_r^2 = w_{mm}/w_{mm}^{mod}$ is the ratio of the concordance model prediction to the one in the corresponding model. We choose
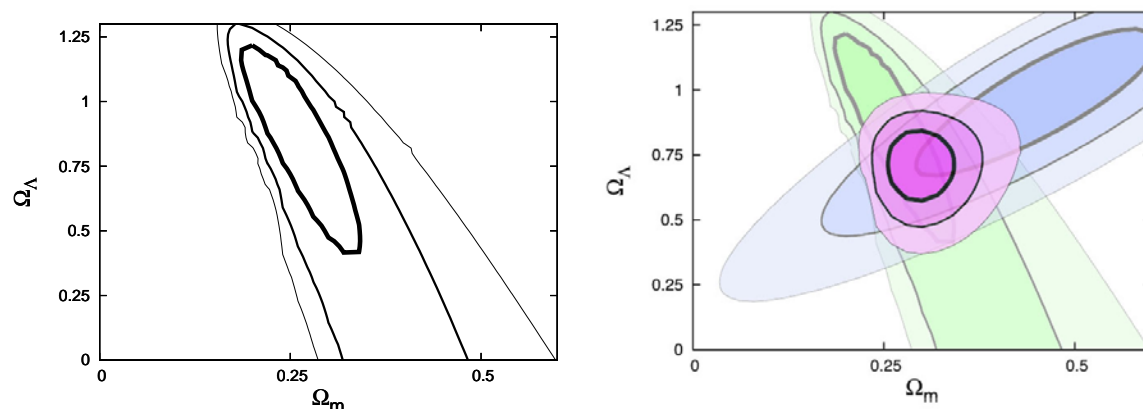
Figure 10.2: One, two and three sigma confidence contours in the $(\Omega_m, \Omega_\Lambda)$ plane (marginalized over h) for the ΛCDM model. Left: constraints from only ISW. Right: constraints from SNIa (blue) and ISW (green) along with the combined contours (purple). Figure as in Gaztanaga, Manera & Multamaki (2006).

to estimate this relative bias at $R = 8$ Mpc/h, but the actual number has little effect in our final conclusions.

10.3 Results of fitting ISW redshift data

Fig.10.1 compares the w_{TG} observations with predictions for a fixed value of $\Omega_m = 0.3$ and three different values of Ω_Λ. We can see how the shape of the prediction depends on the amount of dark energy. Even though W_{ISW} at $z = 0$ depends only weakly on Ω_Λ, the evolution with redshift depends more strongly on Ω_Λ. For a fixed Ω_m, models with larger values of Ω_Λ evolve more rapidly with redshift to the EdS case, where the ISW effect vanishes. Thus, contrary to what happens at $z = 0$, the lower the value of Ω_Λ (for a fixed Ω_m) the larger the ISW amplitude at high redshifts (see for instance the kernel plotted in figure.9.2).

To test model predictions with the data, we use a standard χ^2-test, $\chi^2 = \sum_i (O_i - T_i)^2/\sigma_i^2$, where O_i and σ_i correspond to the different measurements and errors and T_i correspond to the model. The label i runs for $i = 1$ to $i = 5$ marking the different data points (column 1 in Table 10.1) as we move in redshift. In order to take into account the error in the median redshift we take:

$$\sigma_i^2 = \sigma_w^2 + \left(\frac{d(w_{tg}/b)}{dz}\right)^2 \sigma_z^2 \tag{10.5}$$

where σ_w and σ_z are the errors in the w_{TG}/b and $\bar{z}$ respectively (see Table 10.1). We use the relative χ^2 values, $\chi^2 - \chi^2_{min}$, to define confidence levels in parameter estimation. Left panel of figure 10.2 shows the resulting confidence contours. Taking $T_i = 0$ we evaluate the significance of the combined ISW detection. We find that this null hypothesis is rejected with a very high probability: $P \simeq 99.997\%$ (from $P_{\nu=4}(\chi^2 > 26) \simeq 3 \times 10^{-5}$). We next compute the expected ISW effect and compare it with the observational data within the ΛCDM family of models, where Ω_m, Ω_Λ and h are free parameters (we fix the baryonic content $\Omega_b \simeq 0.05$ and the primordial spectral index $n_s \simeq 1$). We choose to normalize each model by fixing σ_8. To make our results independent of this normalization we will marginalize σ_8 over the range $\sigma_8 = 0.8 - 1.0$ (flat prior used). As we compare w_{GT} normalized to the Concordance model bias, we need to compute the relative bias for other LCDM models as explained in section 10.2). We choose to estimate this at $R = 8 Mpc/h$, but the actual number has little effect in the conclusions. We have also marginalized over h in a flat prior range $h = 0.72 - 0.77$). Our results are not very sensitive to the ranges used for σ_8 and h: increasing these ranges by a factor of two change our contours in less than 20 %.

The best fit using only ISW data corresponds to $\Omega_m \simeq 0.26 \pm 0.08$, $\Omega_\Lambda \simeq 0.82 \pm 0.40$, in agreement with the Concordance cosmology. The left panel of figure 10.2 shows the confidence contours for the ΛCDM model along with the constraints from Barris et al. (2004) SNIa observations. From the figure is clear how the ISW effect gives complementary information compared to supernovae. The combination of both yields $\Omega_m \simeq 0.29 \pm 0.04$, $\Omega_\Lambda \simeq 0.71 \pm 0.13$.

The ISW effect can also be used to constrain the dark energy equation of state parameter. In this case, as suggested by the Concordance Model, we assumed a flat universe. We focus on a constant w parameter and maintain the same flat priors for h and σ_8 ($0.72 < h < 0.77$ $0.8 < \sigma_8 < 1.0$). The left panel of figure 10.3 show the one, two and three sigma contours for the (Ω_m, w) plane using only the ISW data. Joint contours with the SNIa data are shown in the right panel of figure 10.3. Both datasets are also complementary for the w determination. The SNIa data is from (Barris et al. 2004).

Making a joint ISW+SNIa analysis with the flat prior reduces notably the allowed space for the parameters to $w = -1.02 \pm 0.17$ and $\Omega_\Lambda = 0.70 \pm 0.05$. The contours are comparable with other analysis in literature (Sandvik et al. 2004) which combines SNIa with WMAP and SDSS data. The results we found are still in full agreement to the Λ CDM model with $\Omega_\Lambda \simeq 0.7$ and $w = -1$.
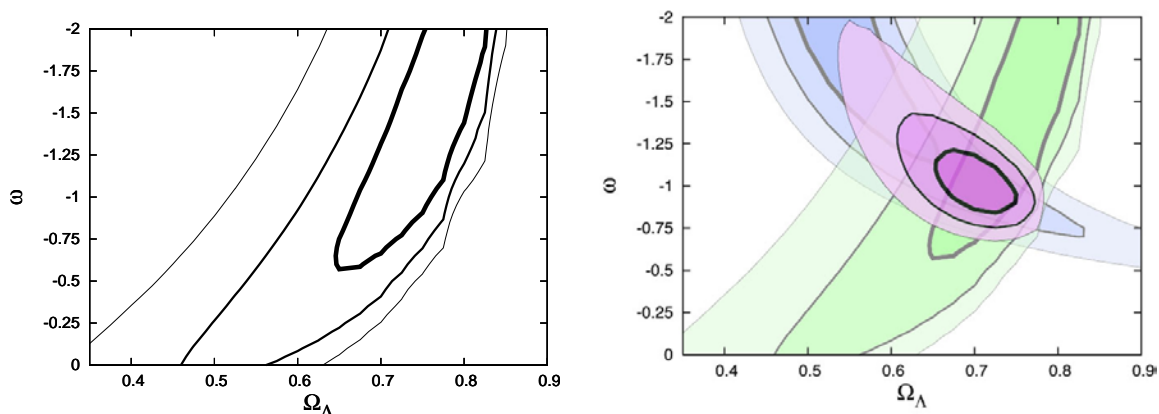
Figure 10.3: One, two and three sigma confidence contours in the (Ω_Λ, w) plane (marginalized over h and σ_8. Left: constraints only from ISW. Right: constraints from SNIa (blue) and ISW (green) along with the combination (purple). Figure as in Gaztanaga, Manera & Multamaki (2006).

10.4 Robustness of the results

10.4.1 Theoretical uncertainties

In this section we explore how robust are our results to the theoretical uncertainties and contaminants. We start looking in the galaxy selection function which is a source of error that must be under control. For the selection function we take a generic parametric form of the type:

$$\phi(z)dz = \frac{\beta}{\Gamma(\frac{m+1}{\beta})} \frac{z^m}{z_0^{m+1}} e^{\left(-\frac{z}{z_0}\right)^\beta} dz \tag{10.6}$$

so that it is normalized to unity. Parameters β and m control the shape of the function and are treat as fix parameters; z_0 is being changed accordingly to the median redshift $\bar{z}$ we want for the selection function. When computing our results we use $\beta = 1.5$ and $m = 2$, in which case $\bar{z} = 1.41z_0$.

In order to clarify the role of the selection function shape we recalculate our results with a much more peaked selection function. This second selection function has $\beta = 2.5$ and $m = 4$ and it is plotted together with the fiducial one in Figure 10.4.1. Both cases have the same median redshift $\bar{z} = 1.41$. Left panel of figure 10.4 shows the contours in the $(\Omega_m, \Omega_\Lambda)$ plane for the more peaked selection function (with $\beta = 2.5$ and $m = 4$). The contours are similar to the fiducial model (ie compare to Fig. 10.2) but favoring slightly lower values for Ω_Λ and Ω_m.

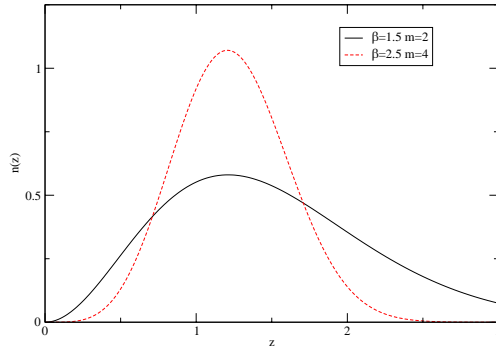Besides the uncertainty on the shape of the selection function there is also uncertainty in the

Figure 10.4: Two different selection functions with the same median redshift $\bar{z} = 1.41$. Both have the generic form given by the equation 10.6. The black continuous line corresponds to $\beta = 1.5$ and $m = 2$ while the red dashed line is for $\beta = 2.5$, $m = 4$

median redshift. We have checked what happens if this uncertainty is not taken into account. We just set the redshift errors $\sigma_z = 0$ in equation 10.5. Contours for the $(\Omega_m, \Omega_\Lambda)$ plane are plotted in the right panel of figure 10.5, which are also to compare with figure 10.2. There is hardly any difference because the theoretical values of w_{TG} change very little within the median redshift error range.

Another source of uncertainty is the use of the gravitational Poisson equation for a flat space instead of a curved one. The correction introduced when one takes into account the curvature is scale dependent and is of order $\frac{H_0^2 \Omega_K}{c^2 k^2}$ (Bardeen 1980; Hu & Eiseinstein 1999) which is subdominant at the angles we are looking and will only slightly change the confidence contours.

There is still another source of error to mention, which is the inclusion of the dipole contribution of the ISW effect in equations 9.11. This contribution should be removed because the WMAP temperature maps does not include it. It actually could enlarge the signal as much as 10%, which, because of the big errors we have, does not modify significatively our results. The outcome would be a little underestimation of the best fit Ω_Λ value.

10.4.2 Possible Contaminants

The constraining power of the new ISW data comes from the simultaneous fitting of data at different redshifts, that is from the shape information in Fig. 10.1. Because of the uncertainties in the relative
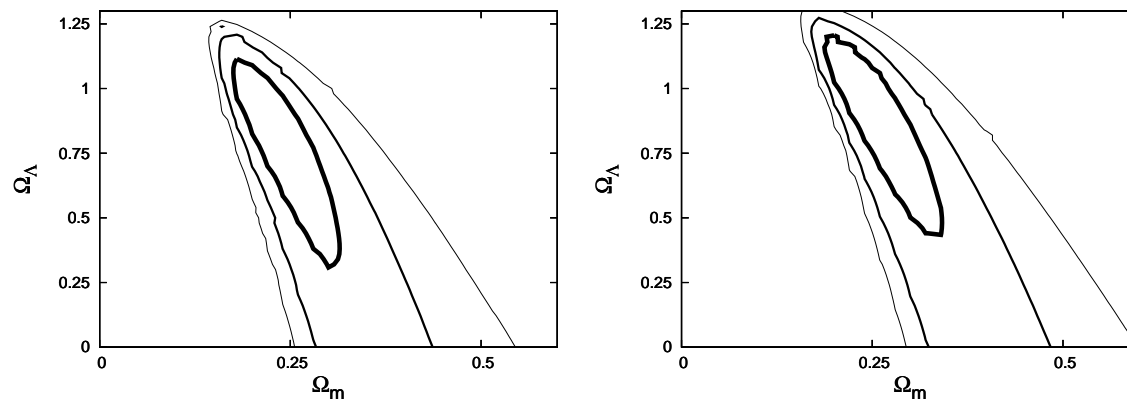
Figure 10.5: One, two and three sigma confidence contours in the $(\Omega_m, \Omega_\Lambda)$ plane for the ΛCDM model. Left panel: contours using a more peaked selection function ($\beta = 2.5$, $m = 4$) but with the same mean redshift as the fiducial case (ie compare to Fig.10.2). Right panel: contours when errors in the median redshift of the selection functions are neglected. Figure as in Gaztanaga, Manera & Multamaki (2006).

normalization due to a relative bias, any given point alone does not constrain well the cosmological parameters. But the combination of the data gives us a new powerful tool for cosmological parameter estimation.

The shape of the curve as a function of redshift also provides an important test for systematics. CMB and galaxy maps are both masked and corrected from galactic absorption/extinction, but any residual contamination could produce a cross-correlation signal. Emission and absorption by our own galaxy produce patchy hot spots in the CMB maps and negative density fluctuations in the galaxy distribution (because of extinction). In principle, this should therefore result in a negative cross-correlation, but overcorrecting for the effects of galactic absorption could also result in a positive signal. This possibility have been tested for each of the samples, by comparing the cross-correlation to WMAP maps at different frequencies. Most analysis use the WMAP Kp0 mask, which excludes about 30% of sky on the basis of galactic or extra-galactic (eg radio sources) contamination. In all cases the contamination seems smaller than the errors (eg see Fig. 2 in Fosalba & Gaztanaga 2004). Moreover, one does not expect this effect to have any redshift dependence, contrary to the measurements in Fig. 10.1.

Cold dust in distant galaxies, will also produce patchy hot spots in the CMB maps and positive density fluctuations in the galaxy distribution (could also be negative because of internal extinction). The resulting cross-correlation should trace the galaxy-galaxy auto correlation function, w_{GG}, and
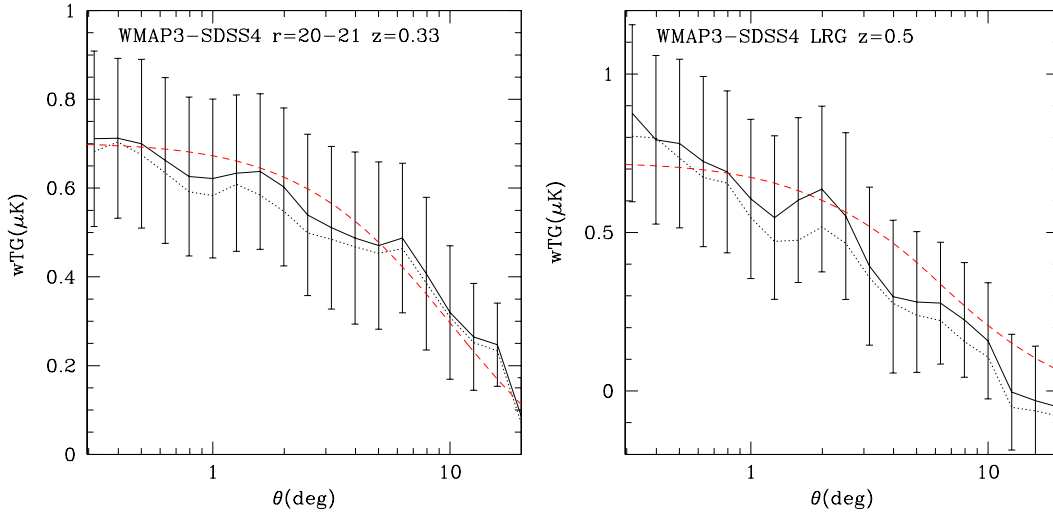
Figure 10.6: The continuous line with errorbars shows the WMAP3-SDSS4 angular cross-correlation as a function of scale for the $z = 0.33$ sample (right panel) and for the $z = 0.5$ sample (left panel). The dotted line corresponds to using the 1st yr WMAP (WMAP1-SDSS4) data, which is very close to the WMAP3 results (continuous line). The dashed lines show the Λ CDM model with $\Omega_\Lambda = 0.83$ (best overall fit) scaled to the appropriate bias and projected to each sample redshift. Figures from Cabre, Gaztanaga, Fosalba, Manera & Castander (2006).

should therefore have a very different redshift dependence to the ISW effect. The dotted line in Fig. 10.1 shows the predicted shape dependence for w_{GG} contamination with arbitrary normalization. The shape is clearly incompatible with the actual cross-correlation measurements. It is also worth noting how w_{GG} goes quickly to zero at $\bar{z} \simeq 0.2$, while the ISW cross-correlation remains positive. This is due to the fact that at these corresponding large scales, about and greater than 40 Mpc/h, the matter-matter correlations w_{mm} effectively decay to zero, while w_{TG}, which traces the gravitational potential, has a less rapid decay with distance.

10.5 Fitting the angular ISW dependence

In the previous sections of this chapter we fit cosmological parameters by means of the ISW effect redshift dependence. In this section we focus in the angular dependence of the crosscorrelation signal and study the significance of the WMAP SDSS crosscorrelation detection.

In figure 10.6 we show the WMAP DR3 and SDSS DR4 angular cross-correlation function for two galaxy samples of different mean redshift. The left panel corresponds to galaxies from a magnitude
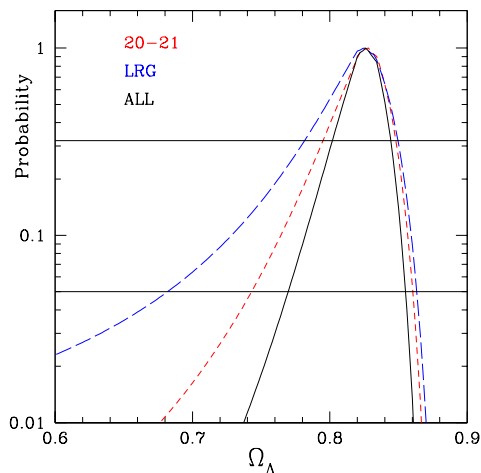
Figure 10.7: Probability distribution: $1 - P_\chi[> \Delta\chi^2, \nu = 1]$ for Ω_Λ in the $r = 20 - 21$ sample (short-dashed line), the LRG sample (long-dashed line) and the combined analysis (continuous middle curve). The range of 68% and 95% confidence regions in Ω_Λ are defined by the intersection with the corresponding horizontal lines. Figures from Cabre, Gaztanaga, Fosalba, Manera & Castander (2006).

$r = 20 - 21$ sample with mean redshift $z = 0.33$, and the right panel to a Luminous Red Galaxy Sample of mean redshift $z = 0.5$. Details of the data cross-correlation and of the selection function can be found at Cabre, Gaztanaga, Fosalba, Manera & Castander (2006). This measurement confirms with a high significance (joint signal to noise $S/N \sim 4.4 - 4.7$) the findings of the WMAP DR1-SDSS DR1 cross-correlation by Fosalba et al 2003.

We proceed to model cross-correlation measurement in Λ CDM cosmology by using equations 9.18 and 9.19. The advantage of these equations is that we can here set the monopole ($l = 0$) and dipole ($l = 1$) contribution to zero, as it is done in the WMAP maps. The $b\sigma_8$ is obtained by fitting the galaxy-galaxy angular autocorrelation measurement to the linear flat Λ CDM model prediction. The power spectrum is $P(k) = A\, k^{n_s}\, T^2(k)$, where $T(k)$ is the Λ CDM transfer function, which we evaluate using the fitting formula of Eiseintein & Hu 1998. As a fiducial parameters (except for the $\Omega_m = 1 - \Omega_\Lambda$ we want to determine) we used the WMAP3 best fit parameters (Spergel et al. 2006) $h = 0.71$, $T_{CMB} = 2.725$, $\Omega_B = 0.022/h^2$, $n_s = 0.938$ and $\Omega_k = 0$ and $\sigma_8 = 0.75\pm^{0.03}_{0.04}$.

To compare models we use a χ^2 test:

$$\chi^2 = \sum_{i,j=1}^{N} \Delta_i\, C_{ij}^{-1}\, \Delta_j, \tag{10.7}$$

where $\Delta_i \equiv w_{TG}^E(\theta_i) - w_{TG}^M(\theta_i)$ is the difference between the "estimation" E and the model M. We perform a Singular Value Decomposition (SVD) of the covariance matrix $C_{ij} = (U_{ik})^\dagger D_{kl} V_{lj}$ where $D_{ij} = \lambda_i^2 \delta_{ij}$ is a diagonal matrix with the singular values on the diagonal, and U and V are orthogonal matrices that span the range and nullspace of C_{ij}. In order to estimate the covariance matrices and errors we have used different prescriptions (which are explained in chapter 11): a) jack-knife, b) 2000 Monte Carlo simulations that include both CMB and their correlated galaxy maps c) theoretical estimation (including cross-correlation signal) both in configuration and harmonic space. For the range of angles we are interested all methods gives very similar results for the Ω_Λ probability distribution.

Fig.10.7 shows the probability distribution estimated for Ω_Λ from the $\Delta\chi^2 = \chi^2 - \chi_{min}^2$ analysis away from the minimum value χ_{min}^2. The combined best fit model has $\Omega_\Lambda \simeq 0.83_{-0.03}^{+0.02}$. The predictions for this Ω_Λ best value are shown as a dashed line in Fig. 10.6. Both samples prefer the same value of Ω_Λ. This is a consistency check for the ΛCDM model. Should this turn not to be so, it would be an indication of a non standard cosmology ($w \neq 1$). It can also be seen (Cabre, Fosalba, Gaztanaga & Manera 2007) that the fit of the equation of state parameter w in a flat cosmology appear to be very degenerate and it is not well constrained with ISW data alone (see also the figure 10.3, and Corasaniti et al. (2005)). Upcoming surveys like DES might help to break the (Ω_Λ, w) degeneracy in the future.

Note that there is a good agreement between the Ω_Λ best fit value obtained in the previous section with ISW data alone (where we looked at the redshift dependence of the ISW signal) with the Ω_Λ best fit value obtained in this section, where the angular dependence of the signal have been fitted. In both cases the ISW alone seems to preffer slightly larger values of Ω_Λ than in the concordance model. However, when ISW is combined with SNIa data (section 10.3) the concordance values are recovered.

Chapter 11

Errors in Cross-correlation Measurements

Summary

In this chapter four different methods for estimating the errors of two sky field cross-correlation measurements are presented. The first method, which has been genuinely developed in this thesis, estimates the error fully in configuration space. This method takes into account the survey geometry and therefore predicts accurate results for large cross-correlation angles. The other methods presented are the theoretical harmonic space errors, the Jack-knife, and the Monte-Carlo errors.

11.1 Theoretical Errors in configuration space (TC)

In this section we present the main formulae of a new method we develop to compute the cross-correlation function between two sky maps in the configuration space. The detailed deduction of this method will be presented in the next two sections. We start with the estimator for the cross-correlation function in the configuration space, which is an average over all θ-separated points in the survey.

$$w_{TG}(\theta) = < \Delta T(q)\delta_g(q')|_{\hat{q}\hat{q}'=\theta} >_{survey} \tag{11.1}$$

107

The formula we have derived for the covariance of this estimator in an ensemble of universe realization is:

$$C_{ij} == \frac{1}{8\pi^2 P(\theta_i)P(\theta_j)} \int_0^\pi \frac{K[\theta_i, \theta_j, \psi]}{P(\psi)} \sin\psi d\psi \qquad (11.2)$$

where the kernel K is given by:

$$\begin{aligned} K[\theta_i, \theta_j, \psi] = &\frac{1}{2}[W_{AA}(\theta_i, \psi)W_{BB}(\theta_j, \psi) + W_{AA}(\theta_j, \psi)W_{BB}(\theta_i, \psi)] \\ &+ W_{AB}(\theta_i, \psi)W_{AB}(\theta_j, \psi) \end{aligned} \qquad (11.3)$$

and W_X is a mean over the corresponding correlation w_X, with $X = TT, GG$ or TG:

$$W_X(\theta, \psi) = 2 \int_0^\pi d\varphi P(\psi, \theta, \phi) w_X(\phi) \qquad (11.4)$$

where $cos\phi = cos\theta cos\psi + sin\theta sin\psi cos\varphi$

The survey geometry is encoded in $P(\theta)$ and $P(\psi, \theta, \phi)$ probabilities. These are the probabilities for two θ-separated points or for a triangle of sides ψ, θ,ϕ to fall completely into the survey area if they are thrown randomly on the whole sky. For compact surveys these probabilities depend mainly of the survey area and can be well approximated by the formulae provided in 11.3.

This new method of computing errors in configuration space have several advantages. Since it takes into account the survey geometry it can provide more accurate errors at large angles where both the jackknife errors and the harmonic-space become inaccurate. Compared to Monte Carlo errors this method is faster because one does not need to generate a large number of sky realizations. One can also decide not to rely in a theoretical model and simply use the direct measured correlation functions to estimate the errors.
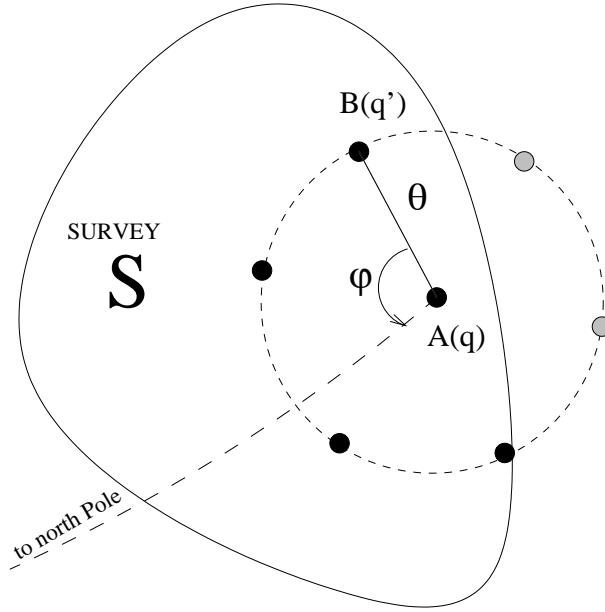
Figure 11.1: Representation of the $\widehat{w}_{AB}(\theta)$ estimator. The two field product AB is averaged in an ordered way over all pairs of θ-separated points that belong to the survey area (black points).

11.2 Deduction of covariance matrix and errors in configuration space

11.2.1 The estimator

Consider two fields in the sky $A(q),B(q')$ which correspond to one realization of the universe. We want to estimate the true two point cross-correlation function of the universe w_{AB} by averaging over the sky in the survey area S. The estimator is

$$\widehat{w}_{AB}(\theta) =< A(q)B(q)|_{\hat{qq'}=\theta} >_S \tag{11.5}$$

where we average over all pairs separated by an angle θ and $\theta + \Delta\theta$ in the survey region. This can be put in an integral form

$$
\begin{aligned}
\widehat{w}_{AB}(\theta) &= \frac{1}{S_N} \int_S dq dq'|_{\hat{qq'}=\theta} A(q)B(q') \\
&= \frac{1}{4\pi 2\pi \sin\theta \Delta\theta P(\theta)} \int_S dq \int_0^{2\pi} \sin\theta \Delta\theta d\varphi A(q) B(q+\theta(\varphi)) D(q,\theta,\varphi) \quad (11.6)
\end{aligned}
$$

Where S_N is the normalization factor and the integral in the second line is over $dq \in S$ and $d\varphi \in (0, 2\pi)$. As it is illustrated in figure 11.1 we integrate all the pairs in an ordered way. Fist we fix a point q and sum over all the θ-separated pairs related to this point. We do this by moving around φ. Since not all points in the sky θ-separated from q belong to the survey we introduce a selection function $D(q, \theta, \varphi)$ which is one if the second point belong to the survey and zero otherwise. We perform this operation in each point of the survey. The origin of φ is not relevant. It could be taken for instance as the direct angle between the θ-pair and the geodesic line between the q point and the pole. The second integration is over all points in the survey.

The normalization factor S_N is a measure of the number of θ-pairs allowed by the survey. This would obviously depend on θ. For an all sky survey S_N would be $4\pi 2\pi \sin\theta \Delta\theta$ The geometry of the survey is enclosed in a multiplicative factor $P(\theta)$, which is actually the ratio between the number of θ-pairs in the survey and the number of θ-pairs in the whole sky, i.e., the probability that when throwing a θ-pair in the whole sky it falls into the survey. When $\theta = 0$ this probability is equal to the fraction of sky f_{sky} covered by the survey. In an all sky survey $P(\theta) = 1$ and also $D(q, \theta, \varphi) = 1$, then the estimator for the cross-correlation is given by:

$$
\widehat{w}_{AB}(\theta) = \frac{1}{4\pi 2\pi} \int dq d\varphi A(q) B(q + \theta(\varphi)) \quad (11.7)
$$

11.2.2 The covariance

In order to get the covariance, we need to relate the estimator of the cross-correlation with the true cross-correlation value. The true cross-correlation value $w_{AB}(\theta)$ is the average over realizations of the estimator, (where the estimator $\widehat{w}_{AB}(\theta)$ is obtained averaging for all the θ-pairs of the sky). Due to homogeneity, $w_{AB}(\theta)$ is also equal to average any θ-pair of fixed points A and B over all the realizations.
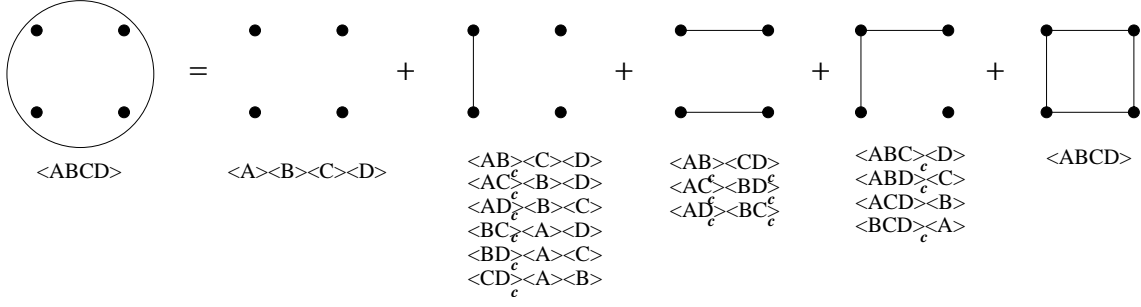
Figure 11.2: Writing the four points moment in 15 terms of connected parts. For a Gaussian field only the two point terms will remain.

$$w_{AB}(\theta) =< \widehat{w}_{AB}(\theta) >_{realization}=< A(q_1)B(q_2) >_{realization} \quad \forall q_1\hat{q}_2 = \theta \tag{11.8}$$

$$\widehat{w}_{AB}(\theta) =< A(q)B(q')|_{q\hat{q}'=\theta} >_{sky} \tag{11.9}$$

where $<>$ means averaging over all the realizations from now on.

The covariance for an arbitrary estimator is

$$
\begin{aligned}
C_{ij} \equiv C_{\widehat{w}}(\theta_i, \theta_j) &=< (\widehat{w}(\theta_1)- < \widehat{w}(\theta_1) >)(\widehat{w}(\theta_2)- < \widehat{w}(\theta_2) >) > \\
&=< (\widehat{w}(\theta_1) - w(\theta_1))(\widehat{w}(\theta_2) - w(\theta_2)) >=< \widehat{w}(\theta_1)\widehat{w}(\theta_2) > -w(\theta_1)w(\theta_2)
\end{aligned}
\tag{11.10}
$$

Thus, for our cross-correlation estimator the covariance is given by

$$
\begin{aligned}
C_{ij} &=< \frac{1}{S_N(\theta_1)} \int_S dq_1 dq_2 \Big|_{q_1\hat{q}_2=\theta_1} A(q_1)B(q_2) \frac{1}{S_N(\theta_2)} \int_S dq_3 dq_4 \Big|_{q_3\hat{q_4}=\theta_2} A(q_3)B(q_4) > \\
&\qquad\qquad\qquad\qquad\qquad\qquad\qquad\qquad\qquad\qquad - w_{AB}(\theta_1)w_{AB}(\theta_2) \\
&= \int_S \frac{dq_1 dq_2 dq_3 dq_4}{S_N(\theta_1)S_N(\theta_2)} \Big|_{q_1\hat{q}_2=\theta_1, q_3\hat{q_4}=\theta_2} < A(q_1)B(q_2)A(q_3)B(q_4) > \\
&\qquad\qquad\qquad\qquad\qquad\qquad\qquad\qquad\qquad\qquad - w_{AB}(\theta_1)w_{AB}(\theta_2)
\end{aligned}
\tag{11.11}
$$

What we are doing in eq (11.11) is fixing four points at the sky (two θ-separated pairs) and average this fixed configuration over realizations of the universe. Then we integrate over all 4-points allowed configurations. The realization average over the four fixed points can be expressed as a sum

of connected terms as it is shown in figure 11.2. For Gaussian fields the four point moment can be simplified and expressed as a function of two-field-correlations.

$$
\begin{aligned}
< A(1)B(2)A(3)B(4) > =&< A(1)B(2) >< A(3)B(4) > + \\
&+ < A(1)A(3) >< B(2)B(4) > + < A(1)B(4) >< A(3)B(2) >
\end{aligned}
$$
(11.12)

where $A(i) = A(q_i)$ and $B(j) = B(q_j)$ and two conditions have to be satisfied

- $< A(i) > = < B(j) > = 0$

- $< A(1)B(2)A(3)B(4) >_c = 0$

Those are very soft requirements. Regarding the first condition we can always modify a field with non zero average to one with zero average just by subtracting its mean (sky averaged) [1] value at each point. The second condition is that the fourth connected moment is zero. This is true for a Gaussian statistics and always a very good approximation for almost Gaussian fields. Note that for fields with zero mean the second moments and the second-connected moments are equal.

Focus for a moment in the first term of equation (11.12). This term has two θ-pairs that are uncoupled. The average over realizations will give, for each pair, the cross-correlation value at the corresponding θ, i.e., $< A(1)B(2) > < A(3)B(4) > = w_{AB}(\theta_1)w_{AB}(\theta_2)$. This value is constant for each 4-point configuration, thus when integrating this term we still got the same result. All in all this term will cancel the last term in equation 11.11. Therefore we only have to calculate two terms:

$$
\begin{aligned}
C_{ij} =& \int_S \frac{dq_1 dq_2 dq_3 dq_4}{S_N(\theta_1)S_N(\theta_2)}\bigg|_{q_3\hat{q}_4=\theta_2, q_1\hat{q}_2=\theta_1} < A(1)A(3) >< B(2)B(4) > \\
&+ \int_S \frac{dq_1 dq_2 dq_3 dq_4}{S_N(\theta_1)S_N(\theta_2)}\bigg|_{q_3\hat{q}_4=\theta_2, q_1\hat{q}_2=\theta_1} < A(1)B(4) >< A(3)B(2) >
\end{aligned}
$$
(11.13)

We have to choose convenient variables to integrate. They will be differ slightly for the first and second integral. Figure 11.3 shows how we choose variables. The idea is the following. Lets stay in the first case when we have to integrate $< A(1)A(3) >< B(2)B(4) >$. First, we fix one point on the sky which correspond to $A(1)$. Second, we notice that $A(1)$ is related to $B(2)$ because

---

[1] here the sky average mean is the estimator for the true mean

A(3)

B(2)

θ_j φ_4

B(4)

θ_i φ_1

ψ

A(1)

case

<A(1)A(3)><B(2)B(4)>

A(3)

θ_j

B(2) ψ' φ_3

B(4)

φ_1
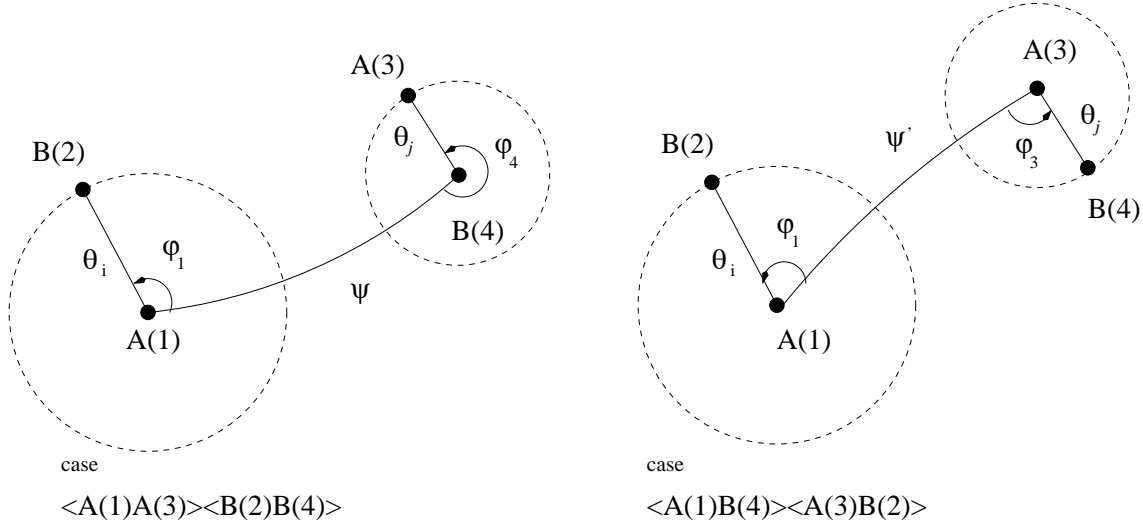
θ_i

A(1)

case

<A(1)B(4)><A(3)B(2)>

Figure 11.3: Variables for integrating equation 11.13.

they are a θ-pair and is related to $A(3)$ because they are to be cross-correlated over realizations. Then we decide to fix distance ψ to the third point $B(4)$. Doing this we have partly decoupled the integrations. Now the cross-correlation pairs only depend on two angles ψ and one φ_i ,i.e, $< A(1)A(2) >= w_{AA}(\phi(\psi, \varphi_4))$ and $< B(2)B(4) >= w_{BB}(\phi'(\psi, \varphi_1, \theta_i))$. Here ϕ and ϕ are the angles between $\hat{1,3}$ and $\hat{2,4}$ respectively. The same idea about what variables to use in the integration is applied over the $< A(1)B(4) >< A(3)B(2) >$ term.

In order to make our deduction clearer we will follow our explanation for an all sky survey. Afterwards we will comment on the case when only a fraction of the sky area is allowed. So, for an all sky survey we easily separate the two θ-pairs having

$$
C_{ij} =
$$
$$
\frac{1}{(4\pi 2\pi)^2} \int_{4\pi} dq_1 \int_0^\pi 2\pi sin(\psi)d\psi \left[\int_0^{2\pi} d\varphi_4 w_{AA}(\phi(\psi, \varphi_4, \theta_2)) \right] \left[\int_0^{2\pi} d\varphi_1 w_{BB}(\phi'(\psi, \varphi_1, \theta_1)) \right] +
$$
$$
\frac{1}{(4\pi 2\pi)^2} \int_{4\pi} dq_1 \int_0^\pi 2\pi sin(\psi)d\psi \left[\int_0^{2\pi} d\varphi_3 w_{AB}(\phi(\psi, \varphi_3, \theta_2)) \right] \left[\int_0^{2\pi} d\varphi_1 w_{AB}(\phi'(\psi, \varphi_1, \theta_1)) \right]
$$
$$
(11.14)
$$

When doing the average over realizations we have lost the dependence on where in the sky we put the 4-points configuration and only the distances between points remain important. We will get

4π from the dq_1 integration. Also, if preferred, due to the symmetry in φ, $\int_0^{2\pi} d\varphi \to 2\int_0^\pi d\varphi$

Using spherical trigonometry we can relate the angular distance ϕ for the cross-correlation $w_X(\phi)$ with their related angles φ, ψ and θ. The relation is given by the cosinus law in spherical trigonometry

$$cos(\phi) = cos(\psi)cos(\theta) + sin(\psi)sin(\theta)cos(\varphi) \tag{11.15}$$

We arrive to the following equations:

$$C_{ij} = \frac{1}{8\pi^2}\int_0^\pi sin\psi d\psi [W_{AA}(\theta_j,\psi)W_{BB}(\theta_i,\psi) + W_{AB}(\theta_j,\psi)W_{AB}(\theta_i,\psi)] \tag{11.16}$$

$$W_X(\theta,\psi) = \int_0^{2\pi} w_X(\phi)\big|_{cos\phi=cos\theta cos\psi + sin\theta sin\psi cos\varphi}d\varphi \tag{11.17}$$

where X stands for any two field combination AA,AB,BB. When estimating the covariance the true value of w_X have to be substituted by its estimated value.

By construction the covariance is symmetric in its arguments, i.e, $C_{ij} = C_{ji}$. This symmetry still remains in equation (11.16) but it is hidden. It remains because we integrated over all four points configurations. It is hidden because of the chosen coordinates for the integration. When integrating we privilege some points over others. We separate the integral by fixing two ψ-separated points and integrating over φ angles. If the points chosen to be ψ-separated were $B(2)$ and $A(3)$ instead of $A(1)$ and $B(4)$ we would have ended by equation (11.16) with $\theta_1 \leftrightarrow \theta_2$. Although the symmetry exists we find it convenient to put it more explicitly. In equation (11.16) we change the kernel to

$$K[\theta_i,\theta_j,\psi] = \frac{1}{2}[W_{AA}(\theta_i,\psi)W_{BB}(\theta_j,\psi) + W_{AA}(\theta_j,\psi)W_{BB}(\theta_i,\psi)]$$
$$+ W_{AB}(\theta_i,\psi)W_{AB}(\theta_j,\psi) \tag{11.18}$$

11.2.3 Partial sky survey

Probability considerations

In most cases our survey only has a restricted area of the sky to estimate the cross-correlation signal. If we throw a point, the probability that it falls into the survey area is the fraction of the sky covered

by the survey area f_{sky}. We define $P(\theta)$ as the probability that a randomly thrown θ-pair in the sky falls (both points) into the survey area. This probability can also be understood as the ratio between the number of θ-pairs of this survey and the total θ-pairs in the sky. The conditional probability $P(\theta/1p)$ that both points of the θ-pair are inside the survey, once we know that one is already inside, is given by

$$P(\theta/1p) = \frac{P(\theta)}{f_{sky}} \tag{11.19}$$

We define that $P(\psi, \theta, \phi)$ as the probability that the triangle of sides ψ, θ, ϕ falls (all) inside the survey area when thrown randomly in the sky. The conditional probability that the third point of a triangle falls into the survey when we know that the other two points, ψ-separated, are already in, is

$$P(\psi, \theta, \phi/\psi) = \frac{P(\psi, \theta, \phi)}{P(\psi)} \tag{11.20}$$

It is also useful to remember that $S_N(\theta) = 4\pi 2\pi \sin\theta \Delta\theta P(\theta)$ is the normalization factor for the estimator

Probabilities for $P(\theta)$ and $P(\psi, \theta, \phi)$ are to be computed for each survey geometry. In the section 11.3 we compute those probabilities for a polar cap survey, i.e., a survey which contains all points with distances less that r to a given point (the pole). A polar cap geometry is a very useful approximation for most cosmological surveys, which are compact and extend to a wide area. For those surveys we can use the probabilities $P(\theta)$ and $P(\psi, \theta, \phi)$ in section 11.3.

The covariance integration

We are in the case of limited area of the sky. In this case when computing the covariance one has to integrate only the 4-point configuration allowed in that area. We focus in the first term of equation (11.13) that we named I_1 We replace the integration over the survey configuration by the integration over all sky configurations convolved with a delta-selection function D which selects the

configurations in the survey.

$$
\begin{aligned}
I_1 &= \int_{4\pi} \frac{dq_1 dq_2 dq_3 dq_4}{S_N(\theta_1) S_N(\theta_2)} D(q_1, q_2, q_3, q_4) < A(1)A(3) >< B(2)B(4) > \\
&= \frac{1}{S_N(\theta_1) S_N(\theta_2)} \int_{4\pi} dq_1 D(q_1) \int_0^\pi d\psi \int_0^{2\pi} d\alpha sin(\psi) D(q_4)) \\
&\left[\int_0^{2\pi} d\varphi_4 \sin\theta_2 d\theta_2 w_{AA}(\phi(\psi, \varphi_4, \theta_2)) D(q_3) \right] \left[\int_0^{2\pi} d\varphi_1 \sin\theta_1 d\theta_1 w_{BB}(\phi'(\psi, \varphi_1, \theta_1)) D(q_2) \right]
\end{aligned}
$$

$$(11.21)$$

where α is the angle between ψ-pair and the line from q_1 to the pole. The other angles are as in figure (11.3). In the above expression we have formally split $D(q_1, q_2, q_3, q_4)$ into four parts $D(q_1)D(q_2)D(q_3)D(q_4)$ which in fact have the same meaning: they are unity only when all the 4 points are inside the survey and they are zero otherwise.

This is an exact result for the I_1 term. The key point here is to approximate the integrals over D's by replacing those selection functions D by a convenient probability. Here we are throwing all 4 points in an ordered way. We throw the first point at q_1. $D(q_1)$ will select if it fall in the survey area. The substitution $D(q_1) \rightarrow f_{sky}$ applies here. Next point to be thrown is q_4 which is ψ-related to q_1. We substitute $D(q_4)$ by $P(\psi/1p)$, i.e, the probability that once a point is in the survey area a second point ψ-separated also falls into. The next two points q_2 q_3 are not related between them but they are related to the two previous points already thrown. $D(q_2)$ and $D(q_3)$ are to be substituted by the probability that, given two points ψ-separated exists in the survey, a third point is also in the survey at distances θ and ϕ to those previous points. $D(q_3)$ is substituted by $P(\psi, \theta_2, \phi/\psi)$, and $D(q_2)$ by $P(\psi, \theta_1, \phi'/\psi)$. When expanding the normalization factors and doing the trivial integrals we get:

$$
\begin{aligned}
I_1 &= \frac{1}{4\pi 2\pi P(\theta_1) P(\theta_2)} f_{sky} \int_0^\pi d\psi sin(\psi) P(\psi/1p) \\
&\left[\int_0^{2\pi} d\varphi_4 w_{AA}(\phi(\psi, \varphi_4, \theta_2)) P(\psi, \theta_2, \phi/\psi) \right] \left[\int_0^{2\pi} d\varphi_1 w_{BB}(\phi'(\psi, \varphi_1, \theta_1)) P(\psi, \theta_1, \phi'/\psi) \right]
\end{aligned}
$$

$$(11.22)$$

Unfortunately, by replacing $D \rightarrow P$ we (slightly) break the symmetry $\theta_1 \leftrightarrow \theta_2$. Thus for the covariance we will use the kernel in equation (11.18) which will recover this symmetry. Replacing the conditional probabilities for non-conditional ones we arrive to the final result.

$$C_{ij} = \frac{1}{8\pi^2 P(\theta_1)P(\theta_2)} \int_0^\pi \frac{K[W]}{P(\psi)} sin\psi d\psi \tag{11.23}$$

$$K[W] = \frac{1}{2}[W_{AA}(\theta_1,\psi)W_{BB}(\theta_2,\psi) + W_{AA}(\theta_2,\psi)W_{BB}(\theta_1,\psi)] + W_{AB}(\theta_1,\psi)W_{AB}(\theta_2,\psi) \tag{11.24}$$

$$W_X(\theta,\psi) = \int_0^{2\pi} P(\psi,\theta,\phi)w_X(\phi)\big|_{cos\phi=cos\theta cos\psi+sin\theta sin\psi cos\varphi}d\varphi \tag{11.25}$$

Small angle approximation

In this approximation θ_1 and θ_2 are small. We can consider that when one point of the θ-pair falls into the survey the other also does. It corresponds to $P(\psi,\theta,\phi) \to P(\psi)$, while $P(\theta) \to f_{sky}$. In this approximation we can express W_X in terms of the all sky one $W_X = P(\psi)W_X^{allsky}$, where the expression for W_X^{allsky} is in equation 11.17. Then we get

$$C_{ij} = \frac{1}{8\pi^2 f_{sky}^2} \int_0^\pi P(\psi)K[W^{allsky}]sin\psi d\psi \tag{11.26}$$

Note that $P(\psi) = f_{sky}$ for $\psi = 0$ and decreases until zero for the maximum correlation angle allowed in the survey ψ_{max}. If the Kerenel $K[W]$ decreases very rapidly and is very small at the scales where $P(\psi)$ significantly deviates from f_{sky} then we can approximate also $P(\psi)$ by f_{sky}. For instance, this is the case of the crosscorrelation between CMB temperature maps and galaxy surveys when $\psi_{max} >> 5\,deg$. In figure 11.4 we plot, for a polar cap survey of 10% of the sky and $\theta_1 = \theta_2 = 0.3$, the functions $P(\psi)$ and $K[W(\psi,\theta_1,\theta_2]sin(\psi)$. This last one arbitrarily scaled for convenience and we can see that is very peaked near $\psi \simeq 0$. Thus, with the mentioned approximation we have $C_{ij} \simeq \frac{C_{ij}^{allsky}}{fsky}$ and consequently

$$C_{ii} = \sigma(\theta) \simeq \frac{\sigma^{allsky}}{\sqrt{(f_{sky})}} \tag{11.27}$$

This is the popular approximation of error scaling as $\propto \frac{1}{\sqrt{f_{sky}}}$ that is commonly used in the harmonic space theoretical error.
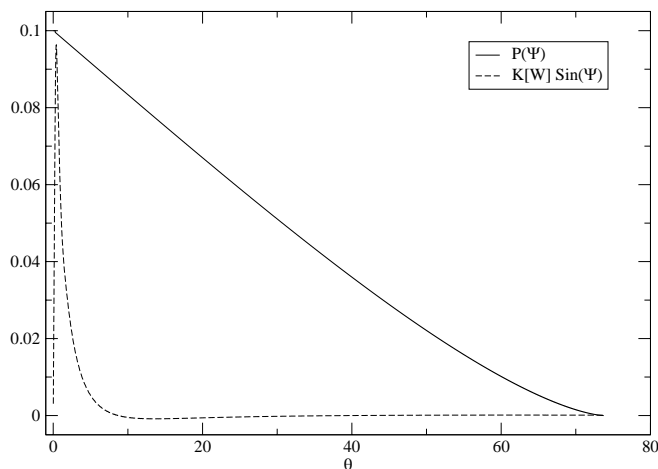
Figure 11.4: Small angle approximation for a $f_{sky} = 0.1$ polar cap survey. Solid line is $P(\psi)$ and dash line $k[W(\psi, \theta_1, \theta_2]sin(\psi)$ for $\theta_1 = \theta_2 = 0.3deg$ The latter is arbitrarily scaled for convenience and we can see that is very peaked near $\psi \simeq 0$, which means that we can approximate $P(\psi) = P(\psi = 0) = f_{sky}$ in equation 11.26.

11.3 Probabilities of finding pairs, triangles, and polynomials in a polar cap survey

Let us place a given θ-pair or a spherical triangle $\Delta(\theta, \psi, \phi)$ randomly on a sphere. In this section we compute the probabilities of finding them inside a polar cap survey of area A.

A polar cap of radius r is the union of all points of an sphere with (spherical) distances less than r to a given point (the pole). The Area of a polar cap is:

$$A = 2\pi R^2[1 - \cos(r)] \tag{11.28}$$

where R is the radius of the sphere. We set it equal to one as usually in spherical trigonometry.

The probability of a N-points polygon to be thrown inside a polar cap of radius r is equal to the intersection area of N circles of radius r, each one centered in one of the polygon (vertex) points, normalized to (divided by) the total area of the sphere, i.e., 4π .

How is it so? The probability for a given polygon to be thrown inside a circle of radius r (polar
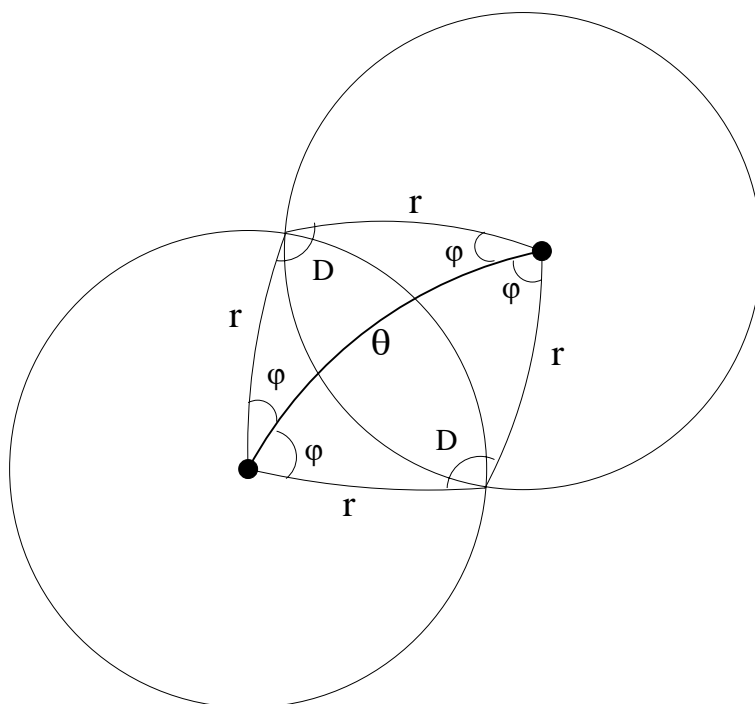
Figure 11.5: Geometry for the intersection of two spherical circles. It is needed in order to determine the $P(\theta)$ probability

cap) already in the sphere is the same as the probability of first drawing the polygon in the sphere and then throwing the circle and finding it encompassing all N-points (vertex). For this to happen the center of the circle must be at a distance less than r for any of the polygon points. Only those points in the area intersected by N circles of radius r, one from each vertex, holds this condition. So this area contains the fraction of points in the sphere that, if they were a center of a polar cap survey, would contain the polygon. Then, the probability of finding the polygon inside a polar cap survey of radius r is that area divided by the total area of the sphere. This closes the demonstration.

11.3.1 Probability for a θ-pair: $P(\theta)$

As we have seen, the probability for a θ-pair thrown randomly on a sphere to fall inside a circle of radius r (polar cap survey) is:

$$P(\theta) = \frac{\left(\begin{array}{c}\text{intersection area of two circles radius } r \\ \text{separated a distance of } \theta\end{array}\right)}{4\pi} \tag{11.29}$$
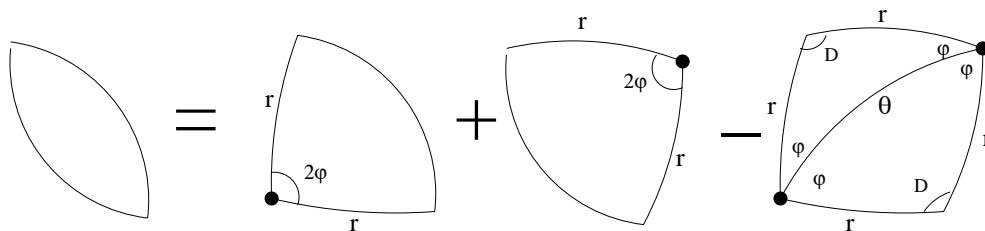
119

Figure 11.6: Representation of how to obtain the intersection area of two spherical circles from sectors of spherical circles and spherical triangles.

Two compute the area of the intersection, A, we make use of the figures 11.5 and 11.6 as well as spherical trigonometry formulae. When $\theta > 2r$ there is no intersection and the probability $P(\theta)$ is zero. When $\theta < 2r$ and $2r + \theta < 2\pi$ we construct two symmetrical triangles $\Delta(\theta, r, r)$ as shown in the figure 11.5 The area of the intersection is given by the sum of two sectors of spherical circle minus the area of those triangles. In spherical trigonometry the area of a triangle is given by the sum of the angles between its sides minus π. Thus

$$A = [2\varphi(1 - \cos(r))] + [2\varphi(1 - \cos(r))] - [2(\varphi + \varphi + D - \pi)] = 2\pi - 2D - 4\varphi\cos(r) \qquad (11.30)$$

where D and φ are given by the cosinus law and semiperimeter half angle formulae

$$\cos(D) = \frac{\cos(\theta) - \cos^2(r)}{\sin^2(r)} \qquad (11.31)$$

$$\tan(\frac{\varphi}{2}) = \sqrt{\frac{\sin(s - r)\sin(s - d)}{\sin(s)\sin(s - r)}} = \sqrt{\frac{\sin(r - \theta/2)}{\sin(r + \theta/2)}} \qquad (11.32)$$

$$s = \frac{\theta + r + r}{2} \qquad (11.33)$$

When $\theta < 2r$ but $2r + \theta < 2\pi$ (and therefore $r > \pi/2$) the two r-circumferences do not intersect each other although the two circles area still overlap. The area of the intersection is all the sphere except the area of the two complementary circles, i.e.,

$$A = 4\pi - [4\pi - 2\pi(1 - cos(r))] - [4\pi - 2\pi(1 - cos(r))] = -4\pi cos(r) \qquad (11.34)$$
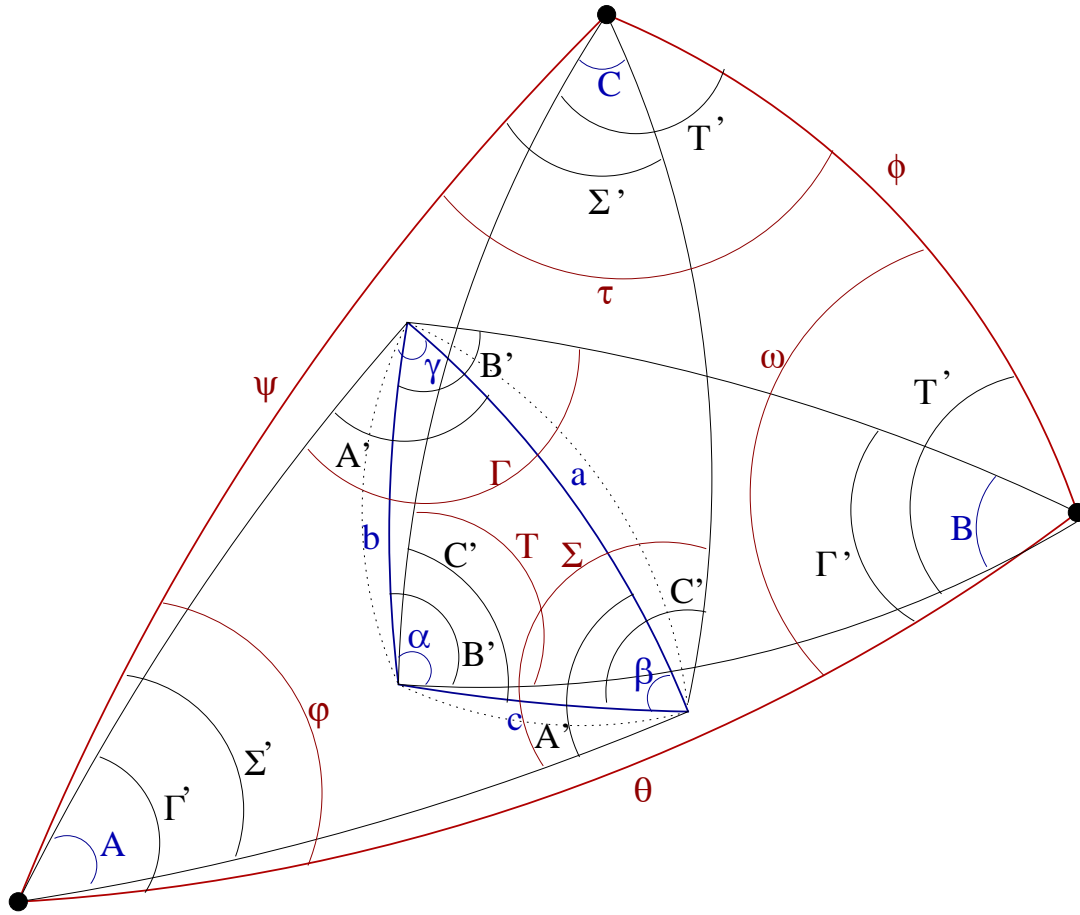
Figure 11.7: Geometry for intersection area of three circles of radius r centered at the three black points. Angles shown in the figure are used in equation 11.37 to compute the intersection area. This is directly related to the probability $P(\psi, \theta, \phi)$.

11.3.2 Probability for a triangle $\Delta(\psi, \theta, \phi)$: $P(\psi, \theta, \phi)$

As we have seen, the probability for a triangle $\Delta(\psi, \theta, \phi)$ thrown randomly on a sphere to fall inside a circle of radius r (polar cap survey) is:

$$P(\psi, \theta, \phi) = \frac{\binom{\text{intersection area of three circles radius } r}{\text{centered at the vertex}}}{4\pi} \qquad (11.35)$$

When the intersection does not exist $P(\psi, \theta, \phi) = 0$. This is the case if $r < \rho_o$, where ρ_o is the radius of the spherical circumference that circumscribes the triangle $\Delta(\psi, \theta, \phi)$. It can be shown [2]

---

[2] ρ_o can be deduced by relating the spherical and the Euclidean triangle with the same points for the vertex. The
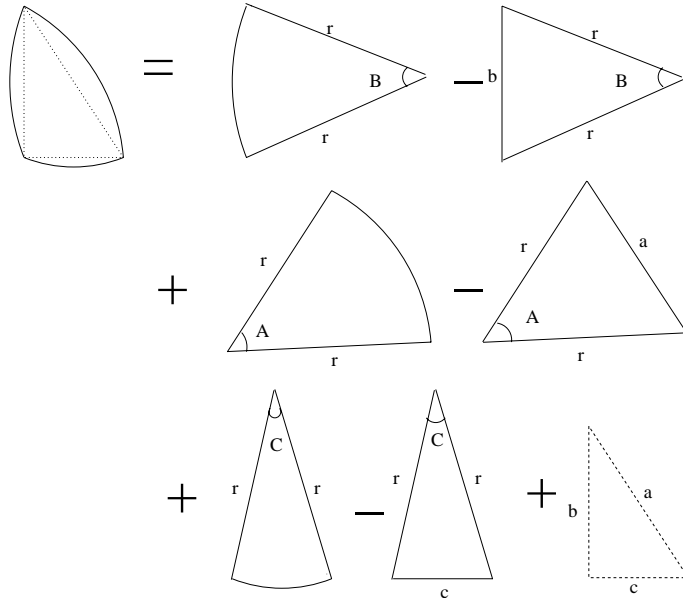
Figure 11.8: Representation of how to obtain the intersection area of three spherical circles from sectors of spherical circles and spherical triangles.

that,

$$sin(\rho_o) = \frac{2\sin(\psi/2)\sin(\theta/2)\sin(\phi/2)}{\sqrt{(S(S-\sin(\psi/2)(S-\sin(\theta/2)(S-\sin(\phi/2))}} \tag{11.36}$$

where $S = \sin(\psi/2) + \sin(\theta/2) + \sin(\phi/2)$ When $\rho_o < r$ and $\rho_o + r < \pi$, the intersection area, A, exist, and to compute it we can make use of the figures in 11.7 and 11.8 as well as spherical trigonometry formulae. The intersection area A is delimited by three arcs of a circle of radius r. Three points mark the intersection of those arcs in the limiting region. One can construct a spherical triangle $\Delta(a, b, c)$ having those points as vertices. This is the blue triangle in figure 11.7, which shows all necessary angles for this section. Figure 11.7 also shows how one can get the area A from the

---

radius of a circumscribed circumference is well known for an Euclidean case $R = \frac{abc}{4\sqrt{s(s-a)(s-b)(s-c)}}$, where s is the semiperimeter of the euclidean triangle with sides a b and c.

triangles an sectors of circles. Following this figure the area is

$$
\begin{aligned}
A &= [B(1 - \cos(r))] - [B' + B' + B - \pi] + [A(1 - \cos(r))] - [A' + A' + A - \pi] \quad (11.37) \\
&+ [C(1 - \cos(r))] - [C' + C' + C - \pi] + [\alpha + \beta + \gamma - \pi] \\
&= 2\pi - \cos(r)(A + B + C) - \Sigma - \Gamma - T \\
&= 2\pi - \cos(r)(2\Sigma' - 2\Gamma' - 2T' - \varphi - \omega - \tau) - \Sigma - \Gamma - T
\end{aligned}
$$

Where we applied that angles $\alpha, \beta, \gamma, A, B, C$ can be expressed as a sum of other angles. The angles left can be obtained by the spherical cosinus law. We write only three here, all other angles can be computed in a similar way.

$$
\begin{aligned}
\cos(\varphi) &= \frac{\cos(\phi) - \cos(\psi)\cos(\theta)}{\sin(\psi)\sin(\theta)} \quad (11.38) \\
\cos(\Sigma) &= \frac{\cos(\psi) - \cos^2(r)}{\sin^2(r)} \\
\cos(\Sigma') &= \frac{\cos(r) - \cos(\psi)\cos(r)}{\sin(\psi)\sin(r)}
\end{aligned}
$$

When $\rho_o < r$ but $\rho_o + r > \pi$ the intersection of the three circles exist but we can not construct such a triangle as in 11.3.2. The area is given by all sky except the sum of the intersection areas of the two points complementary circles, i.e.,

$$
A = 4\pi - 4\pi(1 - P(\psi)) - 4\pi(1 - P(\theta)) - 4\pi(1 - P(\phi)) = 4\pi[P(\psi) + P(\theta) + P(\phi) - 2] \quad (11.39)
$$

11.4   Theoretical Errors in harmonic space (TH)

In this section we present the theoretical errors in harmonic space. In the case of full sky survey they are the simplest because the covariance matrix is diagonal.

In this case, given a spherical harmonic basis, [3] for one sky realization we estimate C_ℓ by

$$C_\ell^{TG} = \frac{1}{2l+1} \sum_m a_{\ell m}^T a_{\ell m}^{G*} = \frac{1}{2l+1} \sum_m a_{\ell m}^{T*} a_{\ell m}^G \qquad (11.40)$$

It is also easy to see that

$$< C_\ell^{TG} C_{\ell'}^{TG} > = \frac{1}{2l+1} \frac{1}{2l'+1} \sum_m \sum_m{}' < a_{\ell m}^T a_{\ell m}^{G*} a_{\ell m}^T a_{\ell' m'}^{G*} > \qquad (11.41)$$

For Gaussian fields we can split the four $a_{\ell m}$ term in pairs, and applying that $< a_{\ell m} a_{\ell m}^* >= \delta_{\ell\ell'}^D \delta_{\ell\ell'}^D$ and $a_{\ell m}^* = (-1)^m a_{\ell -m}$ we can straightforwardly compute the covariance matrix

$$
\begin{aligned}
Cov(C_\ell^{TG}, C_{\ell'}^{TG}) &= < (C_\ell^{TG} C_\ell^{TG}) - < C_{\ell'}^{TG} > < C_{\ell'}^{TG} > \\
&= \frac{1}{(2l+1)} \left[(C_\ell^{TG})^2 + C_\ell^{TT} C_\ell^{GG} \right] \delta_{\ell\ell'}^D.
\end{aligned}
\qquad (11.42)
$$

As expected the covariance in the full sky is diagonal, i.e., there is only variance in the power spectrum. The equation indicates that the variance estimator results from quadratic combinations of the auto and cross power. Using the Legendre transform 9.19 (or 11.49) we can propagate the variance from the harmonic space to the configuration space.

$$
\begin{aligned}
C_{ij} &= Cov(w(\theta_i), w(\theta_j)) = < w(\theta_i) w(\theta_j) > - < w(\theta_i) > < w(\theta_j) > & (11.43) \\
&= \sum_{\ell\ell'} \frac{2\ell+1}{4\pi} \frac{2\ell'+1}{4\pi} Cov(C_\ell, C_{\ell'}) P_\ell(cos(\theta_1)) P_{\ell'}(cos(\theta_2)) & (11.44) \\
&= \sum_\ell \frac{2\ell+1}{(4\pi)^2} P_\ell(cos(\theta_1)) P_{\ell'}(cos(\theta_2)) \left[(C_\ell^{TG})^2 + C_\ell^{TT} C_\ell^{GG} \right] & (11.45) \\
&= \sum_\ell \left(\frac{2\ell+1}{4\pi} \right)^2 P_\ell(cos(\theta_1)) P_{\ell'}(cos(\theta_2)) \Delta^2 C_\ell & (11.46)
\end{aligned}
$$

We note that the dominant contribution for to the error and covariance for the temperature-galaxy correlation comes from the auto-power of the fields $C_\ell^{TT} C_\ell^{GG}$ involved in the cross-correlation, whereas the cross-correlation signal $(C_\ell^{TG})^2$ only gives a few percent contribution, depending on cosmology and survey selection function.

---

[3]Note that one can work also in a real spherical harmonic basis. In this basis, since we are expanding the real valued field, the a_{lm} coefficients will be also real
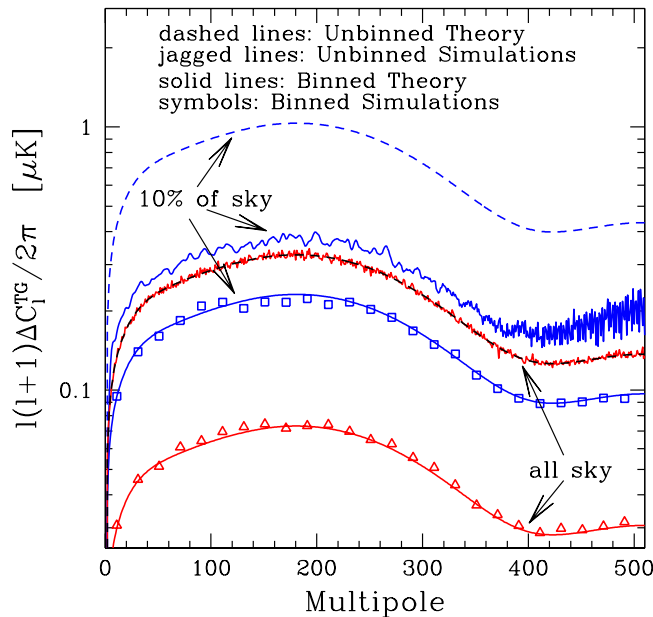
Figure 11.9: Errors in C_ℓ space calculated with (MC2) simulations as compare to (TH-C_ℓ) theory. For all sky maps, the theoretical prediction works well, but for 10% of the sky we see a big discrepancy between theory (dashed lines) and simulations (jagged lines). This is due to covariance between modes and can be solved by binning the C_ℓ spectrum, as shown by the symbols (simulations) and sold line (predictions in Eq.11.47). Figure from Cabre, Fosalba, Gaztanaga & Manera (2007).

11.4.1 TH errors with a fraction of sky area

When we have a fraction of sky f_{sky} at first order the amplitude for the variance in equation 11.42 can be approximated by $f_{sky}(2\ell + 1)$, which is o measure of the number of independent m-modes available to estimate the power at scale ℓ. We shall emphasize that this is only approximate and rigorously it is only expected to yield accurate predictions for azimuthal sky cuts and pairs computed only in this direction.

Partial sky coverage introduces a boundary which results in the coupling of different ℓ modes: the spherical harmonic basis is no longer orthonormal on an incomplete sky and the C_ℓ covariance matrix has off diagonal contributions.

In figure 11.9 Cabre, Fosalba, Gaztanaga & Manera (2007) have compared MC2 errors (which will be explained below) to TH theory in C_ℓ space. It shows how both errors are hard to distinguish for the case of all sky (middle dashed line matches closely the jagged line). For 10% of the sky the

TH error (upper dashed line) obtained theoretically from Eq.11.42 (with a factor $1/\sqrt{f_{sky}}$ respect to all the sky) is much larger than the MC2 error (upper jagged line) in the simulations. We understand this discrepancy in the variance prediction as a transfer of power from the diagonal to off-diagonal errors. In fact, as we have said, the real covariance for a 10% of sky is highly correlated, i.e, very non-diagonal. Therefore it is not surprising that using equation 11.42 (which is diagonal) errors are not recovered. Fortunately, this is not the end of the story. We can get a better diagonal error estimation by binning C_ℓ in a $\Delta\ell$ that makes the covariance approximately diagonal. When binning by $\Delta\ell$, the theoretical error (TH-Cl) in Eq.11.42 is reduced in quadrature to:

$$\Delta^2 C_\ell^{TG} = \frac{1}{\Delta\ell f_{sky}(2\ell+1)} \left[(C_\ell^{TG})^2 + C_\ell^{TT} C_\ell^{GG} \right], \qquad (11.47)$$

This assumes that the bins are independent. Because of the partial sky coverage, the bins are not independent and the above formula will only be valid in the limit of large $\Delta\ell$.

The above formula has been tested in the fiducial cosmological model for different sky fractions by binning the C_ℓ spectrum in simulations and estimating the error from the scatter in different realizations. It was found that the formula works above some minimum $\Delta\ell$ which roughly agrees with the width of off-diagonal coupling in the covariance matrix. For the 10% of the sky this minimum is $\Delta\ell = 20$. The figure 11.9 shows the results for $\Delta\ell = 20$ for both all sky (triangles) and 10% of the sky (squares). It can be seen that the theoretical prediction in Eq.11.47 (solid lines) works very well in both cases, because the covariance with this binning is approximately diagonal. In this case we can propagate safely the errors in C_ℓ to $w(\theta)$ through equation 11.46.

11.5 Monte Carlo Errors from simulations (MC)

When knowing the underlying cosmological parameters one can estimate errors in the cross-correlation or auto-correlations functions by performing Monte Carlo realizations of sky maps. The error will be given by the dispersion of the cross-correlation measurements. As it is shown in Cabre, Fosalba, Gaztanaga & Manera (2007) one needs at least 700 realizations for variance and the normalised covariance matrix to converge. With 200 realizations the accuracy in the errors would be of 20% while with 1000 it would order of one percent.

Following the approach presented in Boughn et al. (1998) we can simulate two correlated Gaus-

sian fields in the sky. Therefore the Monte Carlo simulations come as pairs of maps. The a_{lm}'s of these maps are given by a combinations of unit variance random Gaussian fields ψ.

$$
\begin{aligned}
a_{\ell m}^T &= \sqrt{C_\ell^{TT}}\,\psi_{1,\ell m}, \\
a_{\ell m}^G &= \frac{C_\ell^{TG}}{\sqrt{C_\ell^{TT}}}\,\psi_{1,\ell m} + \left(C_\ell^{GG} - \frac{[C_\ell^{TG}]^2}{C_\ell^{TG}}\right)^{1/2}\psi_{2,\ell m}
\end{aligned}
\tag{11.48}
$$

Here we called the fields T and G because we are mostly interested in the CMB temperature (T) and galaxy over-density (G) fields correlation, but they could also stand for any other Gaussian fields. The true angular auto and cross correlation functions are obviously known by construction because we have used the C_l's as input.

$$
w(\theta) = \sum_\ell \frac{2\ell+1}{4\pi} C_\ell P_\ell(cos\theta) \tag{11.49}
$$

$$
C_\ell = 2\pi \int_{-1}^1 dcos\theta\, w(\theta)\, P_\ell(cos\theta) \tag{11.50}
$$

where we denote by P_ℓ the Legendre polynomial of order ℓ. To estimate $w_{TG}(\theta)$ from the pixel maps we use:

$$
w_{TG}(\theta) = \frac{\sum_{i,j} \Delta_T(\hat{n}_i)\,\delta_G(\hat{n}j)}{Npairs}, \tag{11.51}
$$

where $\Delta_T = T - To$ stands for temperature fluctuations and δ_G for the galaxy number density fluctuation. The sum extends to all pairs i,j separated by $\theta \pm \Delta\theta$. The Monte Carlo (MC) covariance is then defined from the dispersion of the measurements as:

$$
C_{ij} = \frac{1}{M}\sum_{k=1}^M \Delta w_{TG}^k(\theta_i)\Delta w_{TG}^k(\theta_j) \tag{11.52}
$$

$$
\Delta w_{TG}^k(\theta_i) = w_{TG}^k(\theta_i) - \widehat{w}_{TG}(\theta_i) \tag{11.53}
$$

where $w_{TG}^k(\theta_i)$ is the measure in the k-th simulation (k=1,...M) and $\widehat{w}_{TG}(\theta_i)$ is the mean over M realizations which should be close to the input model. The case i=j gives the diagonal error (i.e, variance).

Another Monte Carlo approach to compute errors in the cross-correlation is to simulate uncor-

related Gaussian maps and compute the error estimator as the dispersion of the measurements. Obviously the mean cross-correlation in this case would be zero. We call this method MC1 and the previous one MC2 because in MC2 the maps are realized in pairs. MC1 is actually well suited for a null test, ie, to look if the detection of a cross-correlation is significant compared with a universe with no cross-correlation. However some groups use MC1 to estimate the errors in the cross-correlation. This would give an error systematically subestimated by about 10% in for the concordance model as we will show in chapter 12.

11.6 Jackknife Errors (JK)

In the JK method the data is grouped in M sub-regions or zones which are meant to be more or less independent, or weakly correlated. It is not adequate here to consider individual points or pixels as sub-regions because they are highly correlated. The number of M sub-regions is not previously fixed in this method and have to be adapted for each case. For instance, in the case of a compact survey of a 10% of the sky we will use in chapter 12 we divide a compact square area in $M = 36$ sub-regions. but we have tried different values for $M = 20 - 80$, and find similar results for the cross-correlation errors. The JK regions need to have roughly equal area and shape. This is important; we have found that the JK method could give unrealistic errors when the areas or shapes are not even.

We then use the fair sample (ie ergodicity) hypothesis to estimate the error and to calculate the covariance for the quantity under study. For each subregion we define a new sub-sample contains all sub-regions but one. This is we take a JK sub-sample to be all the data removing one of this JK zones, this means that when computing the crosscorrelation in each sub-sample we remove all the pairs that fall completely or partially in the JK zone that is removed. To compensate for the correlation between the JK sub-samples, we multiply the resulting covariance by $M - 1$. The covariance for this case is thus:

$$C_{ij} = \frac{M-1}{M} \sum_{k=1}^{M} \Delta w_{TG}^k(\theta_i) \Delta w_{TG}^k(\theta_j) \tag{11.54}$$

$$\Delta w_{TG}^k(\theta_i) = w_{TG}^k(\theta_i) - \widehat{w}_{TG}(\theta_i) \tag{11.55}$$

where $w_{TG}^k(\theta_i)$ is the measurement in the k-th sub-sample $(k = 1, ...M)$ and $\widehat{w}_{TG}(\theta_i)$ is the mean

for the M sub-samples.

A potential disadvantage of the JK error is that one may think that it can not be used on scales that are comparable to the sub-regions size. This is not necessarily so. Rare events (such as superclusters) can dominate sampling errors on all scales even if they only extend over small regions (see Baugh et al. 2004). If JK sub-regions are large enough to encompass these rare events, they can reproduce well errors on all scales. Nevertheless it is clear that a danger with JK errors is that the result could in principle depend on the size and shape of the sub-regions. So this needs to be tested in each situation.

The Jack-knife method is related to the Boostrap method (Press et al. 1992). In the Boostrap method one defines the subsamples (which approach statistically independent realizations) by a random selection of the sub-regions. Note that both the Jack-knife and the Boostrap errors are model independent, i.e., they only depend on the data (eg, the value of the field in a sky pixelized maps), and not on any prior information of the cosmological model.

Chapter 12

Comparing Cross-Correlation Error estimator methods

Summary

In this chapter a detailed comparison between the four methods for the estimator of the error in cross-correlation measurements is performed. Results are presented mostly as in Cabre, Fosalba, Gaztanaga & Manera (2007).

12.1 Motivation

As we have seen in chapter 10 a number of groups have recently obtained the first detections of the ISW effect by cross-correlating low redshift tracers of the large scale structure (LSS) with the cosmic variance limited cosmic microwave background (CMB) maps obtained by WMAP (e.g, Boughn and Crittenden 2004; Nolta et al. 2004; Fosalba and Gaztañaga 2004; Fosalba et al. 2003; Scranton et al. 2003; Afshordi et al 2004, Rassat et al 2006, Cabré et al. 2006). Although current detections are only claimed at the 2-4 σ level, all analyses coherently favor a flat Λ CDM model that is consistent with WMAP observations (Spergel et al. 2006). Moreover, the redshift evolution of the measured signal already provides first constraints on alternative cosmological scenarios (Corasaniti et al. 2005; Gaztañaga, Manera & Multamaki 2006).

131

However, sample variance from the primary CMB anisotropies limits the ability with which one can detect CMB-LSS correlations. For the observationally favored flat Λ CDMmodel, even an optimal measurement of the cross-correlation could only achieve a signal-to-noise ratio of ~ 10 (Crittenden and Turok 1996; Peiris and Spergel 2000; Afshordi 2004). Given the low significance level of ISW detections, a good understanding of the systematic and statistical errors is crucial to optimally exploit CMB-LSS correlation data that will be collected in future surveys such as PLANCK, DES, SPT, LSST, etc., for cosmological purposes (see e.g., Pogosian et al. 2005). Recent work has focused on the impact of known systematics on cross-correlation measurements (Boughn and Crittenden 2005; Afshordi 2004), however no detailed analysis has been carried out to assess how different error estimates compare or what is the accuracy delivered by each of them. So far, most of the published analyses have implemented one specific error estimator (primarily in real or configuration space) without justifying the choice of that particular estimator or quantifying its degree of accuracy.

In particular, most of the groups that first claimed ISW detections (Boughn and Crittenden 2004; Nolta et al. 2004; Fosalba and Gaztañaga 2004; Fosalba et al. 2003; Scranton et al. 2003, Rassat et a 2006) estimated errors from CMB Gaussian Monte Carlo (MC) simulations alone. In this approach statistical errors are obtained from the dispersion of the cross-correlation between the CMB sky realizations with a (single) fixed observed map tracing the nearby large-scale structure. This estimator is expected to be reasonably accurate as long as the cross-correlation signal is weak and the CMB autocorrelation dominates the total variance of the estimator. We have called this error estimator MC1.

Fosalba, Gaztañaga & Castander (2003), Fosalba & Gaztañaga (2004), also used Jack-knife (JK) errors. They found that the JK errors perform well as compared to the MC1 estimator, but the JK error from the real data seems up to a factor of two smaller (on sub-degree scales) than the JK error estimated from simulations. This discrepancy arise from the fact that the fiducial theoretical model used in the MC1 simulations does not match the best fit to the data.

Afshordi et al (2004) criticize the MC1 and JK estimators and implement a purely theoretical Gaussian estimator in harmonic space (which we call TH). However, they did not show why their choice of estimator should be more optimal or validate it with simulations. This criticism to the JK approach has been spread in the literature without any critical assessment. Vielva, Martinez-

Gonzalez & Tucci (2006) also point out the apparent limitations of the JK method and adopted the MC1 simulations instead. However they seem to find that the signal-to-noise of their measurement depends on the statistical method used.

Padmanabham et al. (2005) use Fisher matrix approach and MC1-type simulations to validate and calibrate their errors. They also claim that JK errors tend to underestimate errors because of the small number of uncorrelated JK patches on the sky, but they provide no proof of that.

Giannantonio et al (2006), use errors from MC simulations that follow the method put forward by Boughn et al (1998). In their work the error estimator is built from pairs of simulation maps (of the CMB and large-scale structure fields) including the predicted auto and cross-correlation. This is the estimator we named MC2. They point out that their results are consistent with what is obtained from the simpler MC1 estimator.

In this chapter we compare the different error estimators that have been presented in the previous chapter. They are the Configuration (TC) and Harmonic (TH) theoretical errors, the Monte Carlo simulations (MC2) which are built from pairs of correlated maps (MC2) - the option of fixing the galaxy map and varying only the CMB temperature field is MC1-, and the Jack-knife errors (JK). Once we have errors estimated in one space, it is also possible to propagate them through Legendre transformations onto the complementary space. It is important to make a distinction between the method for the error calculation (i.e., MC, JK, TH, TC) and the estimator onto which the errors are propagated, i.e., in $w(\theta)$ or C_ℓ. In this chapter we will deal only with propagated errors or directly estimated in configuration space, which we will notate by adding w after the method letter.

As we have explained in chapter 11 we are assuming Gaussian statistics in all methods except for the JK. In principle it is also possible to perform the comparison analysis with non-Gaussian statistics but this would require particular non-Gaussian models.

It is worth to realize that the methodology presented in the previous chapter and the results presented here could not only apply to ISW cross-correlation studies, but also to other cross-correlation analyses of different sky maps such as galaxy-galaxy or lensing-galaxy studies.

Note that the study in this chapter has been a collaborative work (Cabre, Fosalba, Gaztanaga & Manera 2007) My main contribution relates mainly to the TC model computation and analysis.

12.2 Comparison of the variance

12.2.1 The fiducial model to compare with

We have run a thousand Monte Carlo simulations where both the galaxy and the CMB maps vary around the fiducial autocorrelation and crosscorrelation model. The fiducial model has the following cosmological parameters: $\Omega_{DE} = 0.7$, $\Omega_b = 0.05$, $\Omega_\nu = 0$, $n = 1$, $h = 0.7$, $\sigma_8 = 0.9$. We have choose the galaxies to be distributed in redshift according to the analytic selection function in equation 10.6 with $\beta = 1.5$ and $m = 2$

$$\phi(z) = \frac{3}{2} \frac{z^2}{z_0^3} e^{-(z/z_0)^{3/2}} \tag{12.1}$$

We choose the median redshift $z_m = 0.33$. By construction $z_m = 1.412 \, z_0$. With this median redshift this selection function could reproduce fairly well the SDSS galaxy sample. Note also that for such selection function, one can show that its width simply scales with its median value, $\sigma_z \simeq z_m/2$. For all the sky we have set the monopole ($\ell = 0$) and dipole ($\ell = 1$) contribution to zero in order to be consistent with the WMAP data.

A thousand simulations are generated using Healpix software, so we have a pixelized map to perform the correlations and errors in configuration space (as well as in harmonic space if wanted). For a survey that not covers all the sky we choose a polar cap area, which is the area of the intersection of an sphere and a cone with an opening angle from the north pole. In the case of $f_{sky} = 0.1$ the opening angle is of 37 degrees. An exception is the JK method in which instead of using a polar cap type area for the survey we use a square like area; this allowed us to have even regions for computing the errors.

By construction, in the limit of infinite number of realizations, the MC2 error from simulations should provide the best approximation to the errors. We have seen that the MC2 covariance converges considerably better than to 5% for 1000 simulations (Cabre, Fosalba, Gaztanaga & Manera 2007), thus we take the MC2 result as our true cross-correlation. The JK error will be computed from the simulations data and for the theoretical TC and TH errors we will use the fiducial input model parameters.

12.2.2 Results

Variance in $w(\theta)$

In figure 12.1 we compare the variance for the different methods, which is the diagonal part of the covariance matrix. This figure is one of the main results of this chapter. For all sky maps (lower lines in the figure) we can see that the three methods used: MC2-w, TC-w and TH-w, yield identical results, as expected. For smaller survey areas we do expect some deviations, because of the different approximations on dealing with the survey boundary. For a survey covering 10% of the sky these 3 methods also agree well up to 10 degrees. At larger scales TH-w (dashed lines) starts to deviate, because boundary effects are in fact not taken into account in this method. The JK error (triangles) has a slope as a function of θ that seems less steep than the other methods, but still gives a reasonably good approximation given that the dispersion in the errors is about 20% (see discussion below). Note how on scales larger than 10 degrees the JK method performs better (ie it is closer to MC2) than the TH-w error. The TC method seems to account well for the boundary effects, as it reproduces the MC2 errors all the way to 50 degrees, where all other methods fail. This is worth to be stressed: the new method we present in this thesis for computing the error theoretically in configuration space (TC) turns out to reproduce well the cross-correlation at big angles where the JK and TH errors fail. This method is also computationally efficient, specially if compared to the MC2 where one needs to perform a thousand realizations and a posteriori compute the mean of a thousand correlations.

If we only use one single realization for the galaxies (MC1, dotted line) the error seems to be systematically underestimated by about 10% on all scales. This bias is expected as we have neglected the variance in the galaxy field and the cross-correlation signal.

The figure also shows a particular case of MC1 with real data from SDSS DR5, which has a similar selection function of the one in our simulations. See details of the cross-correlation in Cabre, Fosalba, Gaztanaga & Manera (2007). This case works surprisingly well and it happens to follow the JK prediction rather than the MC1 prediction, but we believe this is just a fluke, given the dispersion in the errors (see below) and the uncertainties in the fiducial model.
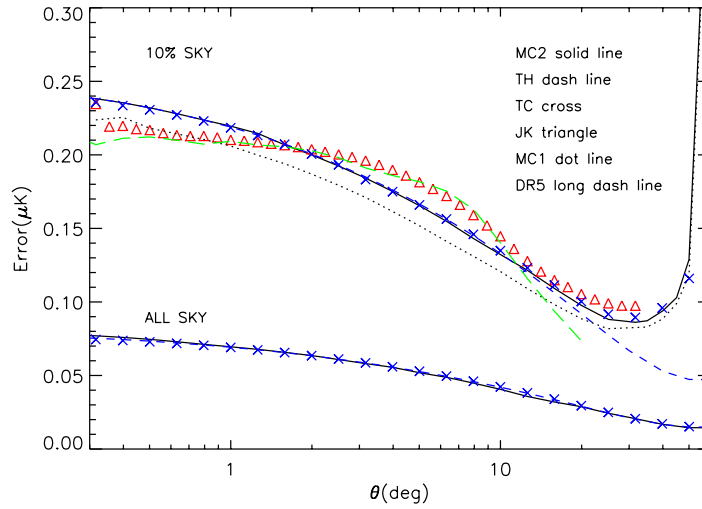
Figure 12.1: Error calculated with different methods (as labeled in the figure) in real space for $\Omega_{DE} = 0.7$. For a map covering 10% of the sky (top lines and symbols), an angles up to 20 degrees, the TC (crosses) and TH (dashed line) theoretical errors work well compared to the Monte Carlo MC2 simulations (solid line), while MC1 simulations (dotted line) seems to underestimate the errors by 10%. The JK method (triangles) seems slightly biased up/down on large/small scales, although all the errors are compatible given the sampling variance dispersion we expect (see Fig. 12.4). Notice that, contrary to the TH errors that always decrease, TC errors reproduce well the MC2 curve inflection at big angles. For all sky maps (bottom lines and symbols), we show how results for MC2 (solid), TH (dashed) and TC (crosses) agree very well. Figure as in Cabre, Fosalba, Gaztanaga & Manera (2007).
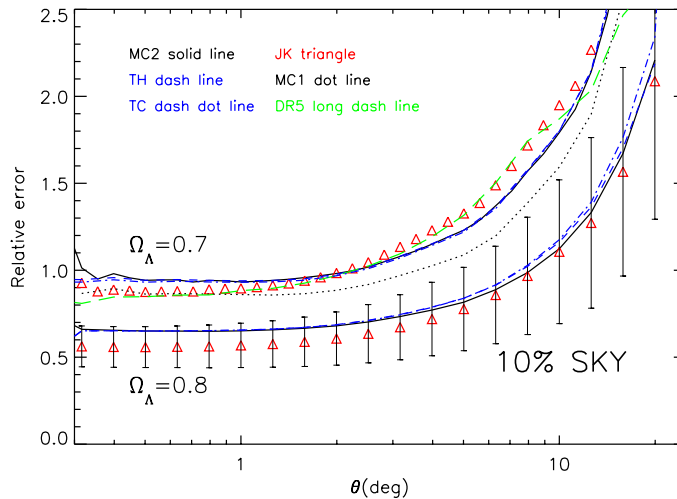

Figure 12.2: Relative error for the two fiducial models $\Omega_{DE} = 0.7$ (top) and $\Omega_{DE} = 0.8$ (bottom). The different methods are labeled in the figure. We see that the relative error depends on the model, and that in the case $\Omega_{DE} = 0.8$ there is also a good agreement within the errors. Figure as in Cabre, Fosalba, Gaztanaga & Manera (2007).
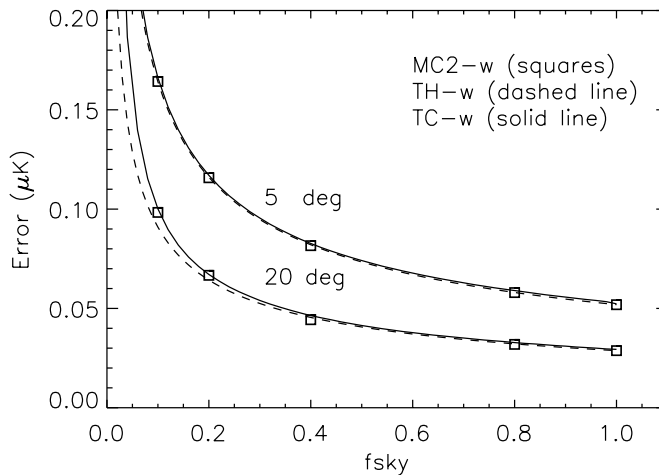
Figure 12.3: Error at a two fix angles: 5 deg (upper lines) and 20 deg (lower lines) as a function of f_{sky}, the fraction of the sky covered by the map. As predicted, errors decrease as $1/\sqrt{f_{sky}}$ in both cases. Note how for small areas, the TC-w prediction (continuous line) performs better than the TH-w model (dashed line) as it better reproduces the MC2 simulations (squares). Figure as in Cabre, Fosalba, Gaztanaga & Manera (2007).

Dependence on Ω_{DE}

We have also studied how our error estimation changes for a different cosmology with $\Omega_{DE} = 0.8$ instead of $\Omega_{DE} = 0.7$. This is shown in figure 12.2. The TC and TH errors still fits well the MC2 predictions, but the JK errors seem to underestimate the errors more than in the $\Omega_{DE} = 0.7$ case. This effect is not large given the dispersion in the errors from realization to realization (errorbars in the figure).

Dependence on f_{sky}

We have tested MC2-w, TH-w and TC-w for different partial sky survey areas f_{sky} and obtained similar results. In Fig.12.3 we have plotted the error for a fix angle of 5 degrees (top) and 20 degrees (bottom) for the different values of f_{sky}. The three methods coincide for large areas. The error scales by a factor $1/\sqrt{f_{sky}}$, as expected.

Notice that errors at angles comparable to the width of the survey are difficult to estimate theoretically because one needs to take into account the survey geometry. Even for a map as wide as 10% of the sky, the survey geometry starts to be important for errors in the cross-correlation above
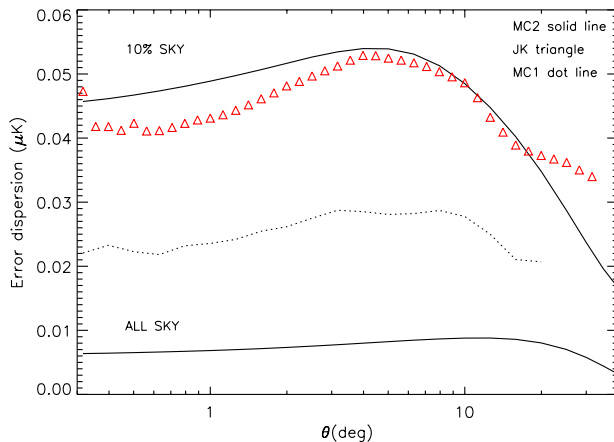
Figure 12.4: Dispersion of the error calculated with different methods in real space for $\Omega_{DE} = 0.7$. For MC2-w (solid line) or MC1-w (dotted lines), we take each pair of MC2 or MC1 simulations as the input for the error in the theoretical method. For JK (triangles), we have one error for each MC2 simulation. We can see how the error in the error is of other 20% for MC2 or JK and is lower for MC1 (mainly because one of the maps in each pair is kept fixed). The lower line corresponds to the dispersion in all sky maps. Figure as in Cabre, Fosalba, Gaztanaga & Manera (2007).

10 degrees. This is shown in simulations as a sharp inflection that begins at 30 degrees in figure 12.1 (solid line) . Our new TC-w method predicts well this inflection, while the more traditional TH method totally misses this feature. This can also be seen in figure 12.3 for 20 degrees when we approach small values of f_{sky}.

Sampling uncertainties in $w(\theta)$

To assess the significance of the differences in the error estimation that we find using different methods, we will compute here the sampling uncertainties associated with error estimation. That is what it is shown in figure 12.4. The sampling dispersion in the error estimates can be calculated from the TH and TC approaches by using C_ℓ or $w(\theta)$ measure in each realization as the input model for theoretical predictions In Fig.12.4 solid (or dotted) line shows the result of using Eq.11.46 for each of the MC2 (or MC1) simulations. This produces an error for each realization and we can therefore study the error distribution. The uncertainty in the error (or error in the error) correspond to the rms dispersion of this distribution.

Note that the error propagation Eq.11.46 is not linear. We find that this produces a bias of 3% when we compare the mean of the propagated errors in each simulation with the propagation of

the mean error in all simulations. We can also calculate the JK-w dispersion of the error, because we have the JK error for each MC2 simulation. As can be seen in figure 12.4 the JK-w dispersion (triangles) is quite close to the MC2-w values.

Uncertainties in the error are then of the order of 20% relative to the mean error. This uncertainty can be interpreted as the result of the uncertainties in our input model; typically the model is only known to the accuracy given by the data and a given sky realization will deviate from the 'true' model (i.e, the mean over realizations). Thus, if one chooses to use the estimated values from the data (or it's best fit model) as input to the error estimation, this produces an uncertainty in the error which is of the order of this scatter. This is always the case with the JK errors, which do not use any model, but the uncertainty is similar if we use direct measurements as input to the other error estimations, as shown in figure 12.4.

For completeness, figure12.4 also shows the dispersion for the MC1 error (dotted). There is less dispersion in the MC1 method because one of the maps is always fixed and this reduces both the error and, more strongly, its dispersion.

12.3 Comparison of the covariance

We have seen in chapter 10 that ISW cross-correlation signal can be used to constrain cosmological parameters, for which it is important to have an accurate understanding of the cross-correlation errors. So far we have compared the variance between different methods. Now we proceed to compare the covariance matrix which plays an important role because the signal at different angles is far from being independent, i.e., it is very correlated.

In figure 12.5 we show the normalized covariance matrix $\widehat{C}_{ij} = \frac{C_{ij}}{\sqrt{(C_{ii}C_{jj})}}$ in configuration space for different methods. At least up to twenty degrees the appearance of the normalized covariance looks like very similar for all methods we used, ie, MC2 TC TH (and JK, which is not plotted), or the fraction of sky. In fact, the all sky normalized covariance matrix is plotted for comparison in the top left panel of figure 12.5. To compare the covariances in more detail we can perform a singular value decomposition. This decomposition will allow us to invert the covariance matrix and ultimately to see whether there are significative differences in these methods when constraining cosmological parameters.
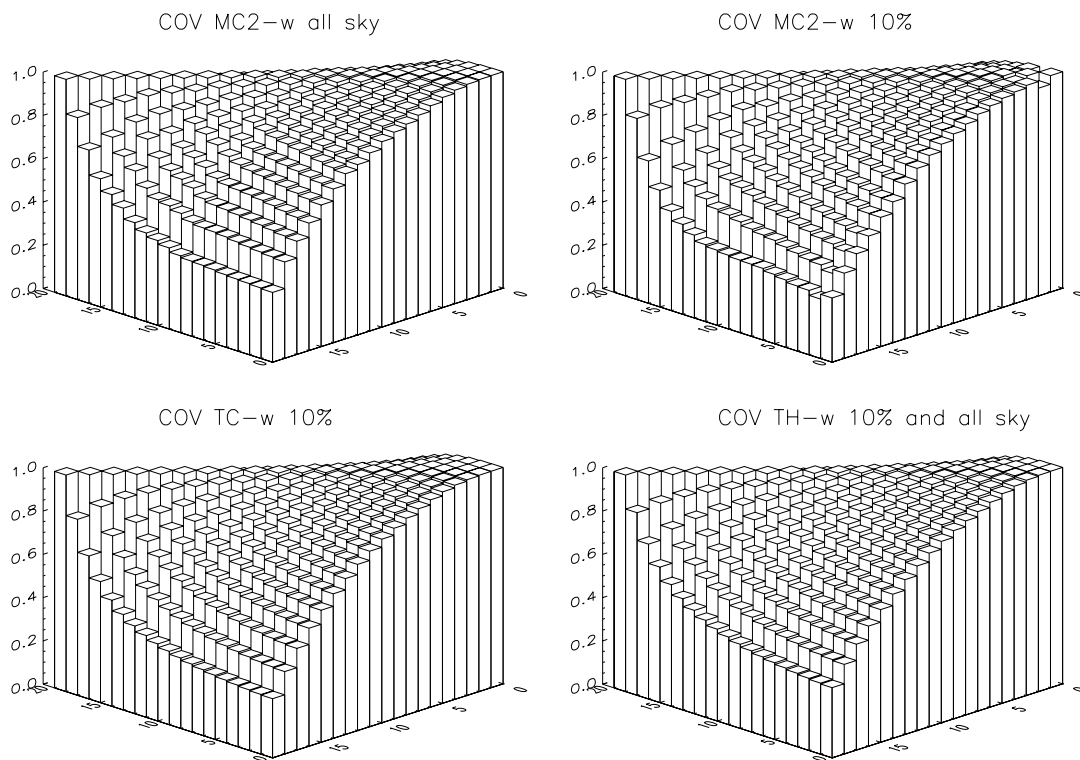
Figure 12.5: Normalized covariances in real space for different methods as labeled in the figure. No significant changes are found for different methods and sky fractions used. Figures as in Cabre, Fosalba, Gaztanaga, & Manera (2007).
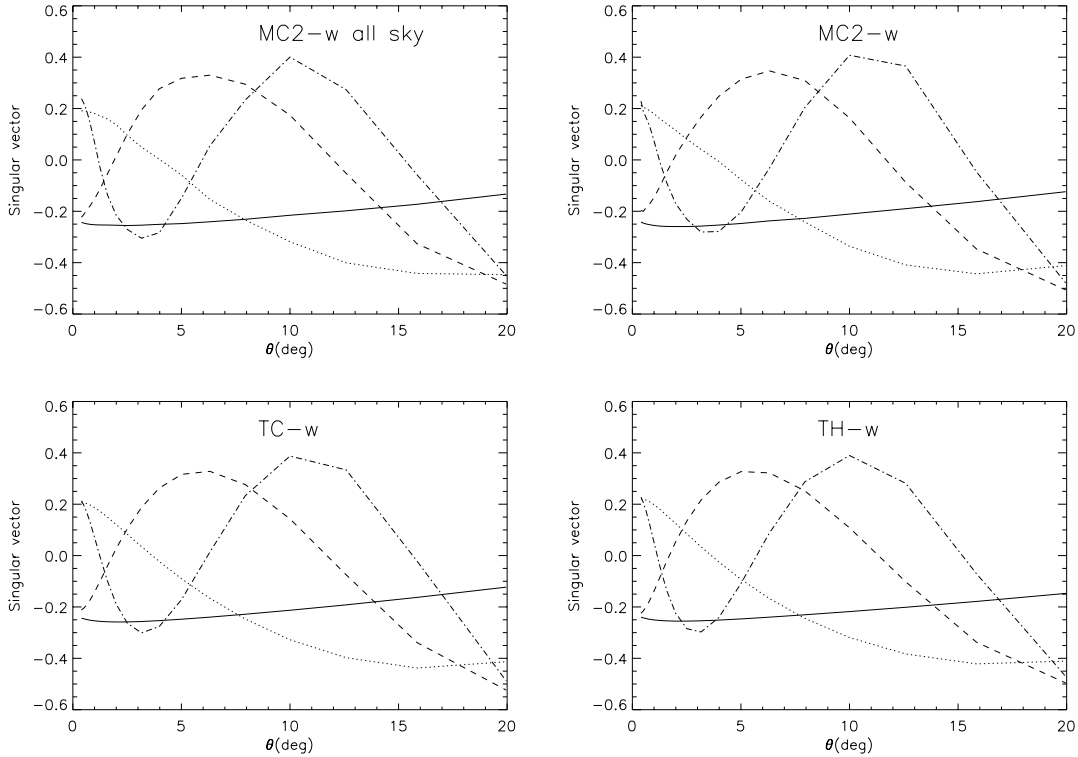
Figure 12.6: Eigenvectors in real space for 10% of the sky and for all sky, as labeled in each panel. First eigenvector is shown as solid lines, second as dotted, third dashed and fourth dot-dash. Results for $MC1-w$ and $TC-w$, not shown here, are very similar. Figures as in Cabre, Fosalba, Gaztanaga & Manera (2007).

The singular value decomposition (see eg Press et al. 1992) decompose the covariance matrix in two orthogonal matrices and a diagonal one, which elements are the square of singular values λ_i. This method is adequate to invert the covariance matrix and to separate the significant contribution to the noise. The later is done by setting the inverses of the small singular values (which are considered noise) to zero. The singular value decomposition method is effectively a decomposition in different modes (egeinvectors and eigenvalues). In Figure 12.6 we show the first four dominant eigenvectors (the ones with higher eigenvalues) as a function of angle, for the TC, TH and MC2 methods. All models (including JK) gives very similar results. From the figure it can be seen that the first mode (solid eigenvector) affects almost only the overall amplitude of the signal, the second mode (dotted) shows a bimodal pattern.

The following modes (dashed and dot-dashed) correspond to modulations on small angular scales.
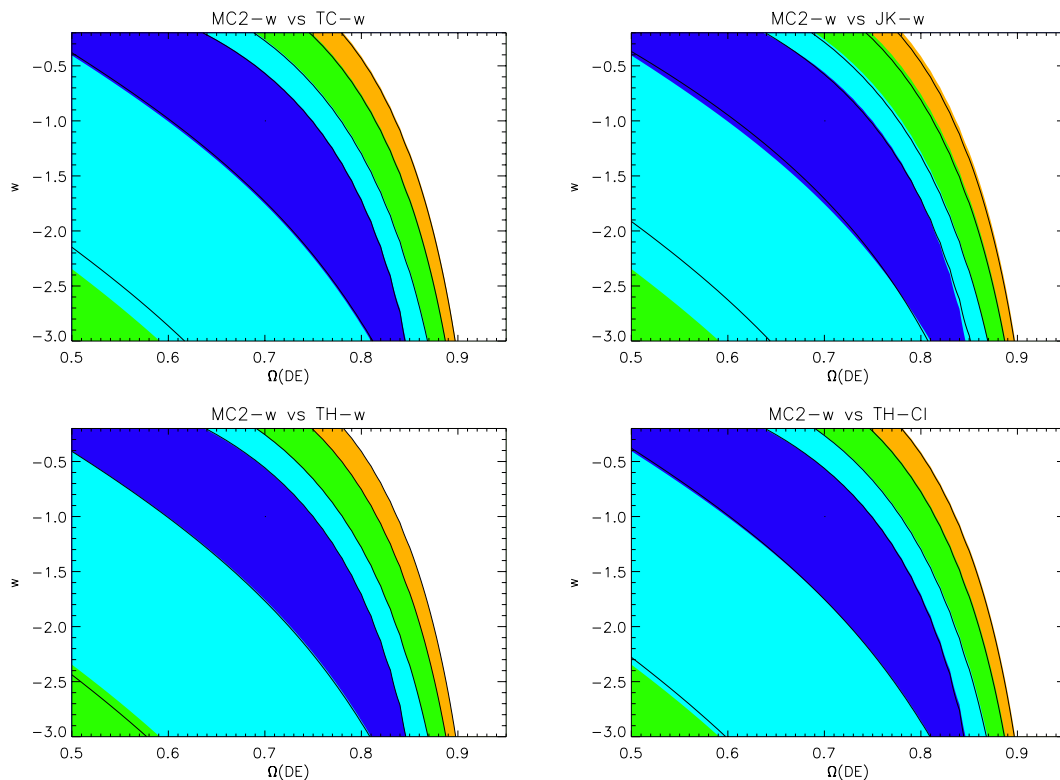
Figure 12.7: χ^2 contours from (MC2-w) simulations (in color) compared to the other methods (solid line): JK-w, MC1-w, TC-w, TH-w, TH-C_ℓ as labeled in each panel. All cases correspond to 10% of the sky. The contour levels are: 0.25, 1., 4. and 9. Figures as in Cabre, Fosalba, Gaztanaga & Manera (2007).

We can project the signal of the fiducial model to the eigenvectors space, thus having a signal s_i for each egeinvector. This would allow us to compute the total signal to noise as $S/N = \sum_i (s_i/\lambda_i)$, which turns out to be 1.2 for the fiducial model with 10% of the sky. In a full sky survey the signal to noise would be 3.8. Obviously the signal to noise is model dependent. Universes with larger values of Ω_{DE} will have large ISW cross-correlation signal and therefore larger (S/N). For a full sky survey in a Λ CDM model with $\Omega_{DE} = 0.8$ we will have $S/N = 5.8$.

Chapter 13

Cosmology with the ISW effect

Summary

In this chapter I summarize the results of the Part II of this thesis, focusing on what we can learn by looking at the ISW effect.

13.1   Summary and Conclusions

In Part II of this thesis we have shown the cross-correlation between CMB-temperature maps and galaxy maps (or other dark matter large scale structure tracers) to be a useful tool for cosmology. In particular the positive detection of the Integrated Sachs-Wolfe effect, must be understood as an independent evidence of the accelerated expansion of the universe (not related to the type Ia SN observations). Even more, not only the ISW effect should be considered a cross-check for confirming the standard cosmology but also a plausible method, despite its error limitations, to point out towards or learn about non-standard forms of dark energy.

In chapter 9 we have presented the dependence of the $w_{TG}(\theta, z)$ ISW signal on both the cosmological parameters (Ω_m, Ω_Λ) and on the equation of state parameter w. The dependence of the W_{ISW} kernel which gives the ISW cross-correlation signal changes with redshift. At low redshift, as expected, the larger the Ω_Λ (for a fixed Ω_m) the higher the signal, while at high redshift it is the opposite.

In chapter 10 we have performed two fits to the Cosmological Parameters. The first one was done

using a compilation of ISW data that covers the whole range of the electromagnetic spectrum (infrared, optical, radio, Xrays) and the second one was done by analysing the angular cross-correlation of two galaxy-samples of the SDSS DR4 with CMB temperature maps. Both fits turned out to give a nice agreement with the Λ CDM model (i.e. no need for $w \neq -1$). The ISW data alone seems to preffer slightly larger values of Ω_Λ than the concordance model, however when we combined ISW and SNIa data the concordance values are recovered.

The compilation we have performed on ISW detections was the first ever presented in the literature. It takes into account only the cases where the bias can be deduced self-consistently from auto-correlations measurements. When comparing data one also has to correct the biases from the fact that they were obtained using different underling fiducial models. When all measurements and their errors are taken together they give new evidence for Dark Energy, being the probability of false detection only $\sim 3 \times 10^{-5}$. The redshift dependence of the ISW signal have been also shown to give complementary results in the (Ω_Λ, w) plane with that of the type Ia supernovae. When performing a joint fit for a flat cosmology we find $\Omega_\Lambda = 0.70 \pm 0.05$ and $w = -1.02 \pm 0.17$. Uncertainties in the selection function and on the possible contaminants were also considered, concluding that they not change significatively the results.

Errors in the ISW cross-correlation measurements are mainly limited by the cosmic variance and the available survey area. Current detections are only claimed to be at the 2-4 σ level and, for the concordance model, and optimal survey could only achieve a signal to noise of about ten. Due to the low significance of the ISW detections understanding the errors becomes a crucial issue. In chapter 11 we presented four different methods to compute the errors and the covariance matrices in cross-correlation measurements. In chapter 12 we compared the different error estimates.

We found that the Monte Carlo method in which both sky maps vary, the Jack-knife method and the theoretical methods either in configuration and harmonic space gave very similar results for diagonal errors and normalized covariance matrices. Consequently the signal to noise and the contours we found when fitting cosmological models were also very similar. We checked that, for angles which are small comparable to the width of the survey, we recover the $1/\sqrt{(f_{sky})}$ dependence of the variance errors. We have also checked that the four methods still give similar results when changing the fiducial Λ CDM model.

The theoretical method for computing errors in configuration space have been genuinely derived

in this thesis. It has the advantage of giving a correct error estimator for angles comparable to the width of the survey, where other methods (Jack-knife, and Harmonic space method) fail. It is also a faster method than the Monte Carlo case where around an order of a thousand pairs of sky maps would have to be generated.

What method shall we use? The Monte Carlo method gives accurate results, but it is expensive in time and uses Gaussian statistics. If the Monte Carlo is performed varying only one of the two sky maps instead of having both maps cross-correlated for each realization, then the errors will be underestimated by about 10%, i.e., about the order of the cross-correlation contribution. The Jack-knife method has the advantage that it does not assume Gaussian statistics and only relies on data and not on an underling model, however its errors might depend on the way it is implemented (the shape and number of sub-regions). The harmonic space theoretical errors are the simplest and the quickest method, but for the partial sky surveys one have to bin in the C_ℓ's appropriately and threat carefully the non diagonal elements. And finally, as have been said, the theoretical method in configuration space is faster than the Jack-knife and Monte-Carlo methods and produces accurate errors for angles comparable to the width of the survey. Note also that although the theoretical and the Monte Carlo errors are model dependent, one could use the best fit data as an input model to make them independent (however this will obviously increase the dispersion of the error estimators within different realizations).